

# Transition from axi- to nonaxisymmetric dynamo modes in spherical convection models of solar-like stars

M. Viviani<sup>1</sup>, J. Warnecke<sup>1,2</sup>, M. J. Käpylä<sup>1,2</sup>, P. J. Käpylä<sup>3,2,1,4</sup>, N. Olsper<sup>2</sup>, E. M. Cole-Kodikara<sup>5</sup>,  
J. J. Lehtinen<sup>1,2</sup>, and A. Brandenburg<sup>4,6,7,8</sup>

<sup>1</sup> Max Planck Institute for Solar System Research, Justus-von-Liebig-Weg 3, D-37077 Göttingen, Germany  
e-mail: viviani@mps.mpg.de

<sup>2</sup> ReSoLVE Centre of Excellence, Department of Computer Science, Aalto University, PO Box 15400, FI-00076 Aalto, Finland

<sup>3</sup> Leibniz Institute for Astrophysics Potsdam, An der Sternwarte 16, 14482 Potsdam, Germany

<sup>4</sup> NORDITA, KTH Royal Institute of Technology and Stockholm University, Roslagstullsbacken 23, SE-10691 Stockholm, Sweden

<sup>5</sup> Department of Physics, Gustaf Hållströmin katu 2a (PO Box 64), FI-00014 University of Helsinki, Finland

<sup>6</sup> Department of Astronomy, AlbaNova University Center, Stockholm University, SE-10691 Stockholm, Sweden

<sup>7</sup> JILA and Department of Astrophysical and Planetary Sciences, Box 440, University of Colorado, Boulder, CO 80303, USA

<sup>8</sup> Laboratory for Atmospheric and Space Physics, 3665 Discovery Drive, Boulder, CO 80303, USA

Preprint online version: December 14, 2024

## ABSTRACT

**Context.** Both dynamo theory and observations of stellar large-scale magnetic fields suggest a change from nonaxisymmetric configurations for rapid rotation to nearly axisymmetric configurations at solar rotation rates.

**Aims.** We seek to understand this transition using numerical simulations.

**Methods.** We use three-dimensional simulations of turbulent magnetohydrodynamic convection in spherical shell segments covering the full 360° longitudinal range and latitudes within  $\pm 75^\circ$ . We consider angular velocities between one and 31 times solar.

**Results.** We find a transition from axi- to nonaxisymmetric solutions at around 1.8 time solar rotation that coincides with the simultaneous change of the rotation profiles from antisolar to solar-like ones. In the solar-like rotation regime, the field configuration consists of an axisymmetric oscillatory field accompanied with the first azimuthal mode  $m = 1$  (two active longitudes), which also shows temporal variability. At slow (rapid) rotation the axisymmetric (nonaxisymmetric) mode dominates. The axisymmetric mode produces latitudinal dynamo waves with polarity reversals, while the nonaxisymmetric mode often exhibits a drift in the rotational reference frame and the strengths of the active longitudes change cyclically over time between the different hemispheres. The latter two phenomena are azimuthal dynamo waves. In the majority of cases we find retrograde waves – in disagreement with observations. The majority of the obtained dynamo solutions exhibit cyclic variability either caused by latitudinal or azimuthal dynamo waves. In an activity–period diagram, the cycle lengths normalized to the rotation period fall on clearly distinct branches as a function of rotation or magnetic activity level. We can clearly identify the inactive branch, but the active and superactive branches appear to be merged into one.

**Conclusions.** As the rotation rate increases, the length scale of convection is decreasing, and the supercriticality of convection is decreasing. The results presented in this paper are the first step to understand dynamos in stars with vastly varying rotation rates, with many new findings, but they also clearly indicate the need for high-resolution simulations in a more supercritical regime with grids that cover full spheres.

**Key words.** Magnetohydrodynamics – convection – turbulence – Sun: dynamo, rotation, activity

## 1. Introduction

Large-scale magnetic fields in late-type stars are thought to be maintained by a dynamo process within or just below the convection zone (e.g. Ossendrijver 2003). In the relatively slowly rotating and magnetically inactive Sun, the dynamo process is often described by a classical  $\alpha\Omega$  dynamo, where shearing due to differential rotation produces toroidal magnetic field from a poloidal one ( $\Omega$  effect), and cyclonic convection ( $\alpha$  effect) is responsible for regenerating the poloidal field (Parker 1955). Younger late-type stars rotate much faster than the Sun and they also exhibit more vigorous magnetic activity. Observations and theoretical models have long indicated that the differential rotation stays roughly constant as a function of rotation (e.g. Kitchatinov & Rüdiger 1999; Reinhold et al. 2013; Reinhold & Gizon 2015). Therefore, the main effect of increased rotation is a relative dominance of the  $\alpha$  effect compared with differential

rotation in maintaining the toroidal field. Hence, in view of dynamo theory (e.g. Krause & Rädler 1980), dynamos in rapidly rotating stars operate in a regime where dynamo action is nearly fully maintained by cyclonic convection ( $\alpha^2$  dynamo). Since the early theoretical work it has been known that in the rapid rotation regime the  $\alpha$  effect becomes increasingly anisotropic (Rüdiger 1978). An indication of this has been seen in wedges at moderate rotation rates (Warnecke et al. 2017). Such an anisotropic  $\alpha$  effect promotes nonaxisymmetric large-scale magnetic field configurations (e.g. Rädler et al. 1990; Moss & Brandenburg 1995; Moss et al. 1995).

Solar and stellar dynamos tend to manifest themselves very differently in observations. The solar magnetic field exhibits cyclic behavior, where the activity indicators vary over an approximate 11 year cycle, and during each activity cycle the polarity of the field reverses, resulting in a magnetic cycle of

roughly 22 years. During one activity cycle, the location in which sunspots are formed migrates from mid-latitudes towards the equator. This is commonly thought to trace the latitudinal dynamo wave, that is a toroidal component of the magnetic field that migrates towards the equator. In the Sun, the longitudinal distribution of sunspots indicates that the solar large-scale magnetic field is mostly axisymmetric (e.g. Pelt et al. 2006). In late-type stars with rapid rotation, by contrast, much larger spots located at high latitudes or even polar regions have been observed using Doppler imaging (DI), Zeeman Doppler imaging (ZDI), and interferometry (e.g. Järvinen et al. 2008; Hackman et al. 2016; Roettenbacher et al. 2016). Many studies have reported on highly nonaxisymmetric configurations of the spots (e.g. Jetsu 1996; Berdyugina & Tuominen 1998), referred to as active longitudes, while especially the indirect imaging of the surface magnetic field using ZDI tends to yield more axisymmetric configurations (Rosén et al. 2016; See et al. 2016).

Especially interesting are the recent results from time-series analysis of photometry obtained by Lehtinen et al. (2016) for a sample of solar-like stars that show a rather sharp transition from stars with magnetic cycles and no active longitudes to ones with both cycles and active longitudes as the activity level or rotation rate of the stars increase. This result can be interpreted in terms of rapid rotators hosting nonaxisymmetric dynamos and moderate rotators axisymmetric ones. Furthermore, some studies have reported on cyclic behavior related to the active longitudes, either in the form of the activity periodically switching from one longitude to the other (Berdyugina et al. 2002) in an abrupt flip-flop event (Jetsu et al. 1993), or irregular polarity changes between the two longitudes, not necessarily in any synchronism (Hackman et al. 2013; Olsper et al. 2015).

The stellar cycles remain poorly characterized, however. Nevertheless, it is clear that many late-type stars exhibit time variability that appears cyclic. This is especially well manifested by studies of stellar samples, such as the intensively investigated Mount Wilson chromospheric activity data base (Baliunas et al. 1995; Oláh et al. 2016). Even if the range of periods that can be studied is severely limited by the nature of the data, it being too short to study long cycles while the rotational and seasonal time scales limit the periods at the short end, it is clear that stellar cycles are common, and even multiple superimposed ones can occur in one and the same object (Oláh et al. 2009; Lehtinen et al. 2016). There are also indications that the stars tend to cluster into distinctive activity branches in a diagram where the ratio of the cycle period over rotation period is plotted against the rotation rate or activity level (Saar & Brandenburg 1999; Lehtinen et al. 2016; Brandenburg et al. 2017), but the existence of these branches continues to raise debate (Reinhold et al. 2017; Distefano et al. 2017).

The steadily increasing computational resources have enabled the large-scale use of self-consistent three-dimensional convection simulations to study the mechanisms that drive dynamo action in stars. Recent three-dimensional numerical simulations have been successful in reproducing many aspects of the solar dynamo, such as cyclic magnetic activity and equatorward migration (e.g. Ghizaru et al. 2010; Käpylä et al. 2012; Augustson et al. 2015), the existence of multiple dynamo modes (Käpylä et al. 2016; Beaudoin et al. 2016), and irregular behavior (Augustson et al. 2015; Käpylä et al. 2016, 2017). There are also studies that investigate the dependence of the dynamo solutions on rotation rate, but these have so far been either limited to wedges (Käpylä et al. 2013, 2017; Warnecke et al. 2016) or the range of rotation rates investigated have been narrow regions in the vicinity of the solar rotation rate (Strugarek et al. 2017)

or three times the solar rotation rate (Nelson et al. 2013). The first indications of stellar dynamos changing from axisymmetric to nonaxisymmetric were reported by Käpylä et al. (2013), Cole et al. (2014), and Yadav et al. (2015), occurring in the regime of moderate rotation. However, the parameter ranges were rather limited in these studies.

Planetary dynamo simulations (e.g. Ishihara & Kida 2000; Schinner et al. 2012; Gastine et al. 2012), which typically have much lower density stratification than their stellar counterparts, show that a transition from multipolar to dipolar magnetic field configurations exists at sufficiently rapid rotation. However, the dipolar solution only exists close to the onset of convection or low density stratification in the study of Gastine et al. (2012). Intriguingly, some ZDI studies suggest that both weak multipolar and strong dipolar magnetic field configurations can occur with very similar stellar parameters in rapidly rotating low mass stars (e.g. Stassun et al. 2011). Numerical simulations have also revealed bistable dynamo solutions in the rapid rotation regime where both configurations can be found with the same system parameters but different initial conditions (e.g. Schinner et al. 2012; Gastine et al. 2012). However, the dipolar solution is typically realized only with a strong initial field. Furthermore, the observational evidence is mostly relevant for fully convective stars or stars with deep convection zones.

The goal of the present paper is to carry out a systematic survey of convective dynamo simulations trying to understand the change of magnetic field generation from a young rapidly rotating Sun to its present rotation rate. We are specifically studying the transition of the dynamo solutions from axisymmetric to nonaxisymmetric ones.

## 2. Model, setup and analysis method

We use spherical polar coordinates  $(r, \theta, \phi)$  to model the magnetohydrodynamics (MHD) in convective envelopes of solar-like stars. The general model and setup are detailed in Käpylä et al. (2013). For most of the runs we use the full azimuthal extent ( $0 \leq \phi \leq 2\pi$ ). However, for some runs we consider only a quarter of the full range ( $0 \leq \phi \leq \pi/2$ ). We omit the poles by including latitudes ( $\theta_0 \leq \theta \leq \pi - \theta_0$ , with  $\theta_0 = 15^\circ$ ), and model only the convection zone of the star in radius ( $0.7R \leq r \leq R$  and  $R$  is the radius of the star).

### 2.1. Basic equations

We solve the compressible MHD equations

$$\frac{\partial \mathbf{A}}{\partial t} = \mathbf{u} \times \mathbf{B} - \mu_0 \eta \mathbf{J}, \quad (1)$$

$$\frac{D \ln \rho}{Dt} = -\nabla \cdot \mathbf{u}, \quad (2)$$

$$\frac{D\mathbf{u}}{Dt} = \mathbf{g} - 2\boldsymbol{\Omega}_0 \times \mathbf{u} + \frac{1}{\rho} (\mathbf{J} \times \mathbf{B} - \nabla p + \nabla \cdot 2\nu \rho \mathbf{S}), \quad (3)$$

$$T \frac{Ds}{Dt} = \frac{1}{\rho} [-\nabla \cdot (\mathbf{F}^{\text{rad}} + \mathbf{F}^{\text{SGS}}) + \mu_0 \eta \mathbf{J}^2] + 2\nu \mathbf{S}^2, \quad (4)$$

where  $\mathbf{A}$  is the magnetic vector potential,  $\mathbf{u}$  is the velocity,  $D/Dt = \partial/\partial t + \mathbf{u} \cdot \nabla$  is the Lagrangian derivative,  $\mathbf{B} = \nabla \times \mathbf{A}$  is the magnetic field,  $\mathbf{J} = \mu_0^{-1} \nabla \times \mathbf{B}$  is the current density,  $\mu_0$  and  $\rho$  are the vacuum permeability and the plasma density,  $\nu$  and  $\eta$  are the constant kinematic viscosity and magnetic diffusivity, respectively.  $\mathbf{g} = -GM\mathbf{r}/r^3$  is the gravitational acceleration

where  $G$  is the gravitational constant and  $M$  is the mass of the star, and  $\Omega_0 = \Omega_0(\cos \theta, -\sin \theta, 0)$  is the rotation vector, where  $\Omega_0$  is the rotation rate of the frame of reference.  $\mathbf{S}$  is rate-of-strain tensor.  $s$  is the specific entropy and equations above are solved together with an equation of state for the pressure  $p$  assuming an ideal gas  $p = (\gamma - 1)\rho e$ , where  $e = c_V T$  is the internal energy,  $T$  the temperature and  $\gamma = c_P/c_V$  is the ratio of specific heats at constant pressure and volume. The radiative and sub-grid-scale (SGS) heat fluxes are given by  $\mathbf{F}^{\text{rad}} = -K\nabla T$  and  $\mathbf{F}^{\text{SGS}} = -\chi_{\text{SGS}}\rho T\nabla s$ , respectively, where  $K$  is the radiative heat conductivity and  $\chi_{\text{SGS}}$  is the SGS heat diffusivity.

## 2.2. Setup characteristics

The initial stratification is isentropic, where the hydrostatic temperature gradient is defined via an adiabatic polytropic index of  $n_{\text{ad}} = 1.5$ . We initialize the magnetic field with a weak white-noise Gaussian seed field. More details about our initial setup can be found in Käpylä et al. (2013).

Most of our runs use a grid extending the full azimuthal extent, but we perform some comparison runs in wedges. In all cases, we assume periodicity in the azimuthal direction for all quantities. For the magnetic field, we apply perfect conductor boundary condition at the bottom and both latitudinal boundaries, at the top boundary we use a radial field condition. Stress-free, impenetrable boundaries are used for the velocity on all radial and latitudinal boundaries. The entropy is controlled by a constant heat flux into bottom of the computational domain. The thermodynamic quantities have zero first derivatives at both latitudinal boundaries, leading to zero energy fluxes there. At the top boundary, the temperature follows a black body condition. The exact equations for these conditions are described in Käpylä et al. (2013, 2017).

Our simulations are defined by the following non-dimensional parameters. As input parameters we quote the Taylor number

$$\text{Ta} = [2\Omega_0(0.3R)^2/\nu]^2, \quad (5)$$

the fluid, SGS, and magnetic Prandtl numbers

$$\text{Pr} = \frac{\nu}{\chi_m}, \quad \text{Pr}_{\text{SGS}} = \frac{\nu}{\chi_{\text{SGS}}^m}, \quad \text{Pr}_M = \frac{\nu}{\eta}, \quad (6)$$

where  $\chi_m = K(r_m)/c_P\rho(r_m)$  and  $\chi_{\text{SGS}}^m = \chi_{\text{SGS}}(r_m)$  are evaluated at  $r_m = 0.85R$ .

Useful diagnostic parameters are the density contrast

$$\Gamma_\rho \equiv \rho(r = 0.7R)/\rho(R), \quad (7)$$

fluid and magnetic Reynolds numbers and the Péclet number,

$$\text{Re} = \frac{u_{\text{rms}}}{\nu k_f}, \quad \text{Re}_M = \frac{u_{\text{rms}}}{\eta k_f}, \quad \text{Pe} = \frac{u_{\text{rms}}}{\chi_{\text{SGS}}^m k_f}, \quad (8)$$

where  $k_f = 2\pi/0.3R \approx 21/R$  is an estimate of the wavenumber of the largest eddies. The Coriolis number is defined as

$$\text{Co} = \frac{2\Omega_0}{u_{\text{rms}} k_f}, \quad (9)$$

where  $u_{\text{rms}} = \sqrt{(3/2)\langle u_r^2 + u_\theta^2 \rangle_{r\theta\phi t}}$  is the rms velocity and the subscripts indicate averaging over  $r$ ,  $\theta$ ,  $\phi$ , and a time interval during which the run is thermally relaxed and which typically covers at least a magnetic diffusion time.

The Rayleigh number is obtained from the hydrostatic stratification, evolving a 1D model, and is given by

$$\text{Ra}_t = \frac{GM(0.3R)^4}{\nu\chi_{\text{SGS}}^m R^2} \left( -\frac{1}{c_P} \frac{ds_{\text{hs}}}{dr} \right)_{(r=0.85R)}, \quad (10)$$

where  $s_{\text{hs}}$  is the hydrostatic entropy.

We define mean quantities as averages over the  $\phi$ -coordinate and denote them by an overbar, for example  $\langle \mathbf{B} \rangle_\phi = \overline{\mathbf{B}}$ . The difference between the total and the mean, for example  $\mathbf{B}' = \mathbf{B} - \overline{\mathbf{B}}$ , are the fluctuations. Furthermore, we indicate volume averages using  $\langle \cdot \rangle_V$ .

For the purpose of this paper, it is convenient to normalize the rotation rate by the solar value, so we define

$$\tilde{\Omega} \equiv \Omega_0/\Omega_\odot, \quad (11)$$

where  $\Omega_\odot$  is the solar rotation rate. Moreover, we use  $\Omega_\odot = 2.7 \times 10^{-6} \text{ s}^{-1}$ , the solar radius  $R = 7 \times 10^8 \text{ m}$ ,  $\rho(0.7R) = 200 \text{ kg/m}^3$ , and  $\mu_0 = 4\pi \cdot 10^{-7} \text{ H m}^{-1}$  to normalize our quantities to physical units.

The simulations were performed with the PENCIL CODE<sup>1</sup>. The code employs a high-order finite difference method for solving the compressible equations of magnetohydrodynamics.

## 2.3. Spherical harmonics decomposition

To investigate the scale dependence of the velocity and magnetic fields, it is instructive to decompose the solutions into spherical harmonics. For this purpose, we will only use the radial components of the magnetic and velocity fields,  $B_r$  and  $u_r$ , respectively. Those are related to the respective superpotentials via

$$B_r = L^2 \mathcal{B}, \quad u_r = L^2 \mathcal{U}, \quad (12)$$

where  $L^2(\cdot) = -\sin^{-1}\partial_\theta(\sin\theta\partial_\theta\cdot) - \sin^{-2}\partial_\phi^2$  is the angular momentum operator and  $\mathcal{B}$  and  $\mathcal{U}$  are the poloidal superpotentials that can be expanded in terms of spherical harmonics  $Y_\ell^m(\theta, \phi)$  as (Krause & Rädler 1980)

$$\mathcal{U}(\theta, \phi) = \sum_{\ell=0}^{\ell_{\text{max}}} \sum_{m=-\ell}^{\ell} \tilde{\mathcal{U}}_\ell^m Y_\ell^m(\theta, \phi), \quad (13)$$

where  $\tilde{\mathcal{U}}_\ell^m$  are computed as

$$\tilde{\mathcal{U}}_\ell^m = \int_0^{2\pi} \int_{\theta_0}^{\pi-\theta_0} \mathcal{U}(\theta, \phi) Y_\ell^{m*}(\theta, \phi) \sin\theta d\theta d\phi, \quad (14)$$

and likewise for  $\tilde{\mathcal{B}}_\ell^m$ . Owing to the absence of magnetic monopoles, however, there is no contribution to the magnetic field for  $\ell = 0$ . In practice, we work directly with the radial components of velocity and magnetic field, whose transforms are related to  $\mathcal{B}$  and  $\mathcal{U}$  via  $\hat{B}_{\ell,r}^m = \ell(\ell+1)\tilde{\mathcal{B}}_\ell^m$  and  $\hat{u}_{\ell,r}^m = \ell(\ell+1)\tilde{\mathcal{U}}_\ell^m$ , respectively.

We decompose the magnetic and velocity field in the first eleven spherical harmonics ( $0 \leq \ell \leq 10$ ) and consider  $0 \leq \ell \leq 5$  and  $0 \leq m \leq 5$  as the large-scale fields and the rest as small-scale fields. Throughout this work we use the decomposition for the radial velocity and magnetic field on a slice at a fixed radial position of  $r = 0.98R$ .

<sup>1</sup> <https://github.com/pencil-code/>

**Table 1.** Summary of the runs.

Run	Grid	$\tilde{\Omega}$	Pr	Pr <sub>SGS</sub>	Pr <sub>M</sub>	Ta	Ra <sub>t</sub>	Re	Pe	Re <sub>M</sub>	Co	$\Gamma_\rho$	$\Delta_\Omega^{(\tau)}$	$\Delta_\Omega^{(\theta)}$
A1	144 × 288 × 576	1.0	58	2.50	1.00	6.32 · 10 <sup>6</sup>	6.54 · 10 <sup>7</sup>	40	100	40	1.6	22	−0.26	−0.37
<b>A2</b>	144 × 288 × 576	1.0	69	0.30	1.00	4.39 · 10 <sup>6</sup>	8.00 · 10 <sup>5</sup>	36	10	36	1.4	21	−0.22	−0.24
<b>B</b>	144 × 288 × 576	1.5	58	2.50	1.00	1.42 · 10 <sup>7</sup>	6.54 · 10 <sup>7</sup>	40	100	40	2.4	22	−0.11	−0.17
C1	144 × 288 × 576	1.8	58	2.50	1.00	2.03 · 10 <sup>7</sup>	6.54 · 10 <sup>7</sup>	41	102	41	2.8	22	−0.08	−0.11
C2	144 × 288 × 576	1.8	58	1.00	1.00	2.03 · 10 <sup>7</sup>	1.29 · 10 <sup>7</sup>	43	43	43	2.6	22	0.78	−0.35
<b>C3</b>	144 × 288 × 576	1.8	77	0.33	1.00	1.14 · 10 <sup>7</sup>	7.00 · 10 <sup>5</sup>	28	9	28	3.0	20	0.07	0.17
D	128 × 256 × 512	2.1	67	3.00	1.00	2.03 · 10 <sup>7</sup>	4.55 · 10 <sup>7</sup>	32	98	32	3.5	26	0.003	0.007
E	128 × 256 × 512	2.9	78	3.50	1.00	2.64 · 10 <sup>7</sup>	3.11 · 10 <sup>7</sup>	25	90	25	5.0	24	0.06	0.06
F1	128 × 256 × 512	4.3	66	3.00	1.00	8.10 · 10 <sup>7</sup>	3.31 · 10 <sup>7</sup>	28	86	28	7.9	23	0.01	0.04
F2	144 × 288 × 576	4.3	57	1.00	1.00	1.17 · 10 <sup>8</sup>	1.29 · 10 <sup>7</sup>	33	33	33	8.3	19	0.03	0.06
F3	144 × 288 × 576	4.3	58	0.25	1.00	1.17 · 10 <sup>8</sup>	9.00 · 10 <sup>5</sup>	27	6	27	9.8	18	0.02	0.07
<b>G<sup>a</sup></b>	256 × 512 × 1024	4.9	43	1.20	1.00	3.47 · 10 <sup>8</sup>	4.55 · 10 <sup>7</sup>	50	61	50	9.3	21	0.03	0.04
<b>G<sup>W</sup></b>	180 × 256 × 128	4.8	67	2.00	1.00	1.25 · 10 <sup>8</sup>	4.00 · 10 <sup>7</sup>	34	68	34	8.3	31	0.05	0.07
<b>H</b>	128 × 256 × 512	7.1	69	3.00	1.00	2.25 · 10 <sup>8</sup>	2.04 · 10 <sup>7</sup>	24	72	24	15.6	21	0.01	0.03
<b>H<sup>a</sup></b>	256 × 512 × 1024	7.8	51	1.40	1.00	6.61 · 10 <sup>8</sup>	5.21 · 10 <sup>7</sup>	40	56	40	16.1	18	0.004	0.014
I	128 × 256 × 512	9.6	71	2.08	1.04	4.63 · 10 <sup>8</sup>	3.93 · 10 <sup>7</sup>	26	55	27	20.4	28	0.01	0.03
<b>I<sup>W</sup></b>	128 × 256 × 128	9.6	71	2.08	1.04	4.63 · 10 <sup>8</sup>	3.83 · 10 <sup>7</sup>	27	56	28	19.9	28	0.01	0.02
J	128 × 256 × 512	14.5	62	2.50	1.00	1.30 · 10 <sup>9</sup>	1.12 · 10 <sup>7</sup>	25	63	25	36.1	18	−0.001	0.01
<b>J<sup>W</sup></b>	180 × 256 × 128	15.5	69	2.00	1.00	1.30 · 10 <sup>9</sup>	3.93 · 10 <sup>7</sup>	21	43	21	41.7	26	0.004	0.009
K1	128 × 256 × 512	21.4	74	3.00	1.00	2.03 · 10 <sup>9</sup>	1.00 · 10 <sup>7</sup>	16	50	16	67.5	13	−0.001	0.007
K2	128 × 256 × 512	21.4	55	2.25	1.00	3.60 · 10 <sup>9</sup>	1.56 · 10 <sup>7</sup>	21	48	21	71.2	13	−0.001	0.005
<b>L<sup>a</sup></b>	256 × 512 × 1024	23.3	60	1.60	1.00	4.6 · 10 <sup>9</sup>	4.58 · 10 <sup>7</sup>	21	32	21	83.4	14.6	0.0001	0.002
<b>L<sup>W</sup></b>	180 × 256 × 128	23.3	70	2.00	1.00	2.92 · 10 <sup>9</sup>	4.00 · 10 <sup>7</sup>	16	33	16	82.4	24	−0.0001	0.003
M	128 × 256 × 512	28.5	61	2.50	1.00	5.18 · 10 <sup>9</sup>	6.00 · 10 <sup>6</sup>	18	46	18	98.7	9	−0.001	0.003
<b>M<sup>W</sup></b>	180 × 256 × 128	31.0	71	2.00	1.00	5.18 · 10 <sup>9</sup>	1.03 · 10 <sup>8</sup>	14	28	14	126.5	21	−0.0001	0.002

**Notes.** Runs in bold are discussed in more detail in the rest of the paper. The quantities in the second to seventh columns are input parameters of the runs whereas the quantities from the eighth to the twelfth column are outcomes of the simulations. The superscript *a* denotes a high-resolution run whereas superscripts *W* denote wedge runs. The horizontal line denotes the transition from axisymmetric (anti-solar) magnetic field (rotation profile) to a nonaxisymmetric (solar) one.

### 3. Results

We consider a number of runs that probe the rotational dependence in the range  $\tilde{\Omega} = 1$ –31, corresponding to  $\text{Co} = 1.6$ –127; see Table 1. For some rotation rates we consider different values of the SGS Prandtl number resulting in different Rayleigh and Péclet numbers. Runs E, F1, and H are direct continuations of Runs A, B, and C of Cole et al. (2014) and Run F1 was already discussed as Run E4 (Käpylä et al. 2013). The wedge simulation Run G<sup>W</sup> has been analysed as Run I in Warnecke et al. (2014), as Run A1 in Warnecke et al. (2016), as Run D3 in Käpylä et al. (2016) and in Warnecke et al. (2017). Furthermore, Runs A1 and A2 correspond to  $2\pi$  extensions of the wedge runs of Set F in Käpylä et al. (2017) whereas Run E corresponds to Set E in Käpylä et al. (2017) and Run B1 in Warnecke et al. (2016). We have also made a selection of models (Runs A2, C3, F3) with a lower Pr<sub>SGS</sub> to compare with other studies where such parameter regimes are explored (e.g. Brown et al. 2010; Nelson et al. 2013; Fan & Fang 2014; Hotta et al. 2016).

#### 3.1. Overview of convective states

All our models have a density stratification that is much smaller than in the Sun. Therefore, the effects of small-scale convection near the surface and the resulting low local Coriolis numbers in those layers are not captured. This can be achieved only at very high resolution (e.g., Hotta et al. 2014) and is not feasible for

parameter studies such as those done here. Thus, the effects of rotation are more strongly imprinted in the velocity field near the surfaces of our models than what is expected in actual stars. This is manifested in Fig. 1 where the radial velocity  $u_r$  is shown for several models with increasing rotation rate. The size of the convection cells at high latitudes decreases as the rotation rate is increased. Also, we observe the appearance of elongated in latitude columnar structures near the equator at about twice the solar rotation rate. These structures, often referred to as banana cells, persist for all higher rotation rates investigated, their azimuthal and radial extents reducing as function of rotation, while the latitudinal extent remains roughly constant. The reason for their emergence is the strong rotational influence on the flow and the geometry of the system. Strong rotation tries to force convection into Taylor-Proudman balance resulting in columnar cells which are aligned with the rotation vector. Such cells are connected over the equator only outside the tangent cylinder in a spherical shell, manifesting themselves as elongated structures at low latitudes. Such convective modes can also lead to equatorial acceleration as observed in the simulations and in the Sun (Busse 1970). In the Sun, the small-scale granulation near the surface masks direct observation of larger-scale convective modes. However, also helioseismic results suggest that large-scale convective structures exceeding the supergranular scale of 20–30 Mm are weak (e.g. Hanasoge et al. 2012).

To quantify the sizes of convective structures as a function of rotation we compute the power spectra of the radial velocity

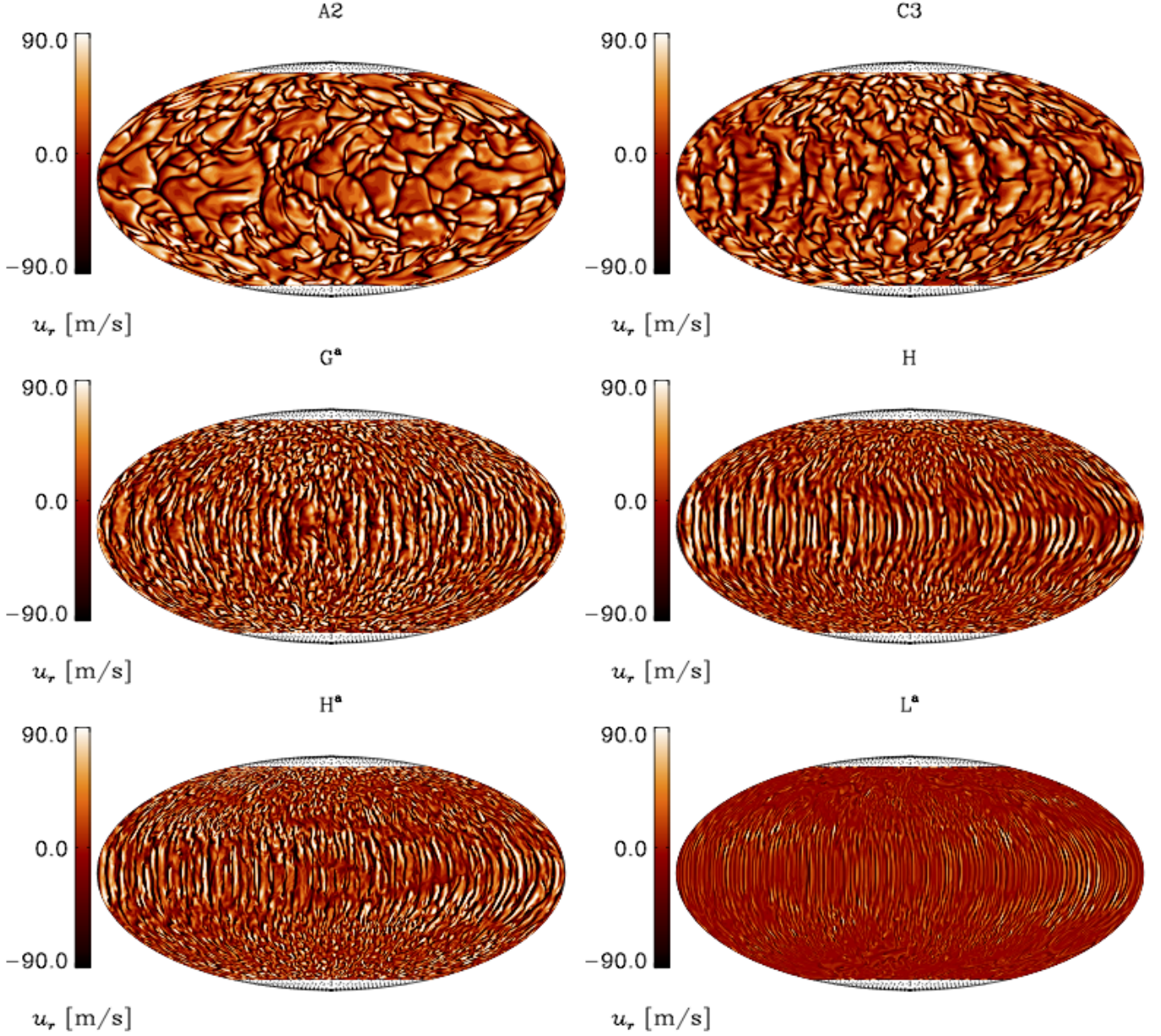


**Fig. 1.** Mollweide projection of radial velocity  $u_r$  at  $r = 0.98R$  for Runs A2, C3,  $G^a$ , H,  $H^a$ , and  $L^a$ .

near the surface, see Fig. 2. The power at each  $\ell$  is

$$P = \frac{E_{\text{kin}}^{(\ell)}}{\sum_{\ell} E_{\text{kin}}^{(\ell)}}, \quad E_{\text{kin}}^{(\ell)} = \sum_{m=0}^{\ell} C_m |\hat{u}_{\ell,r}^m|^2, \quad (15)$$

where  $C_m = 2 - \delta_{m0}$ . We find that for more rapid rotation the radial kinetic energy peaks at smaller scales (higher  $\ell$ s, close to  $\ell = 100$  for Run  $L^a$ ) and the kinetic energy at large scales (lower  $\ell$ ) becomes smaller; see Fig. 2a. The increasing rotational influence is clearly seen in Fig. 2b, where we plot the value of  $\ell$  at the maximum of the radial velocity spectra as a function of the Coriolis number for all runs. The dependence is consistent with a power law with  $\text{Co}^{0.23}$ , which is relatively close to the theoretically expected  $1/3$  scaling for rotating hydrodynamic convection near onset (Chandrasekhar 1961). This dependence is steeper than what was found by Featherstone & Hindman (2016a), who found a slope close to  $1/2$ . Their analysis was done on the horizontal velocity spectra, however.

Next, we look at the energy of the radial velocity field at different values of  $m$ . In Fig. 3 we plot the kinetic energy for  $0 \leq \ell \leq 10$ . While most of the kinetic energy is contained in the small-scales (fourth panel), the nonaxisymmetric  $m = 5$  mode contains most of the energy in the large scale field. Nonaxisymmetric structures in the velocity field are also visible in Fig. 1 around the equator, in particular for Run  $L^a$ . This is in agreement with previous studies (e.g. Brown et al. 2008), which reported the presence of clear nonaxisymmetric large-scale flows for hydrodynamic simulations in parameter regimes near the onset of convection.

### 3.2. Mean flows

To estimate the rotational influence on the convection we also calculated the volume averaged total kinetic energy density and its contributions; see Table 2. The total kinetic energy density is



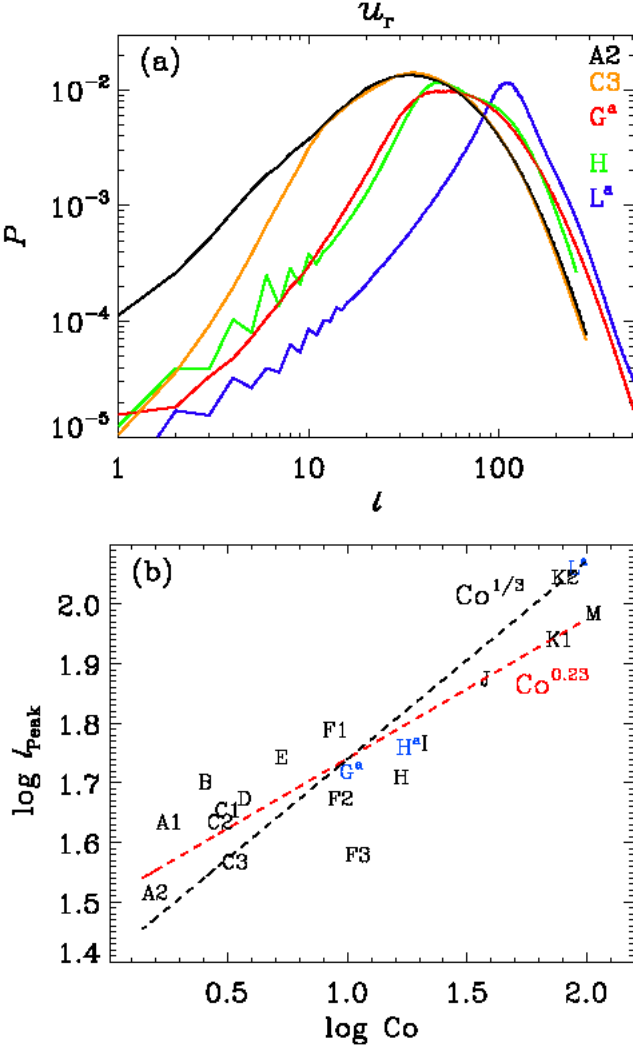


**Fig. 2.** (a) Normalized power spectra  $P$  of the radial velocity as function of degree  $l$  for Runs A2, C3,  $G^a$ , H, and  $L^a$  with increasing rotational influence. (b) Degree of peak power  $l_{\text{peak}}$  estimated from the power spectra plotted over Coriolis number  $Co$ . The runs are indicated with their run names. The red dashed line is a linear fit, the black dashed line is the expected slope from theoretical estimates (Chandrasekhar 1961).

given by

$$E_{\text{kin}} = \langle \frac{1}{2} \rho u^2 \rangle_V, \quad (16)$$

and the contributions contained in differential rotation and meridional circulation are, respectively:

$$E_{\text{kin}}^{\text{DR}} = \langle \frac{1}{2} \rho \bar{u}_\phi^2 \rangle_V, \quad E_{\text{kin}}^{\text{MC}} = \langle \frac{1}{2} \rho (\bar{u}_r^2 + \bar{u}_\theta^2) \rangle_V. \quad (17)$$

The contribution from the nonaxisymmetric fluctuations is

$$E_{\text{kin}}^{\text{fluc}} = E_{\text{kin}} - (E_{\text{kin}}^{\text{DR}} + E_{\text{kin}}^{\text{MC}}). \quad (18)$$

The total kinetic energy decreases nearly monotonically as a function of rotation. This clearly shows the rotational quenching of the convection. That might be related to an increasing critical Rayleigh number in rapidly rotating system, however, we do not find that an increase in Rayleigh number for high resolution runs compensate the rotational decrease. As a result, the flow becomes less supercritical for convection the higher the rotation rate, which is also reflected in the monotonous decrease of

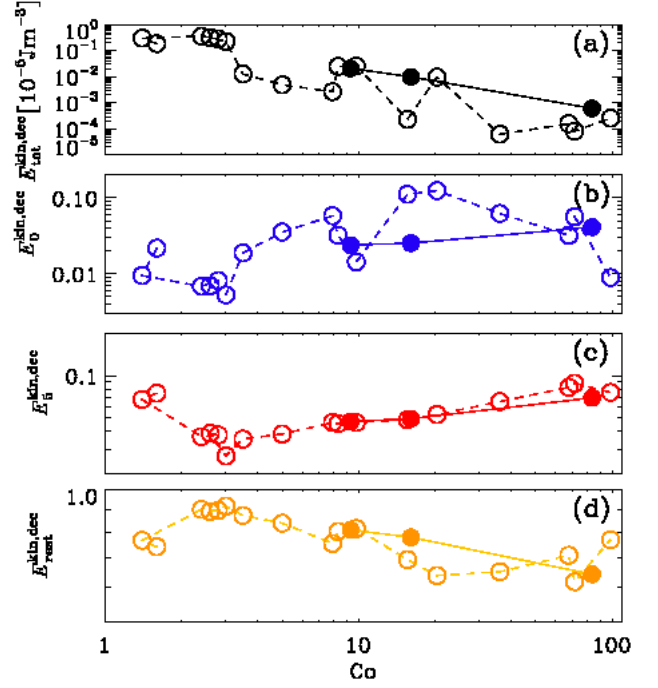


**Fig. 3.** Kinetic energy of the decomposition as a function of Coriolis number  $Co$  for all  $2\pi$  runs showing the total energy (a), the axisymmetric contribution ( $m = 0$ ) (b), the fifth non-axisymmetric mode ( $m = 5$ ) (c) and the small-scale contribution ( $m > 5$ ) (d). Panels b-d are normalized to the total energy (panel a). Filled circles connected by a continuous line indicate high resolution runs.

**Table 2.** Volume averaged kinetic and magnetic energy densities in units of  $10^5 \text{J m}^{-3}$ .

Run	$E_{\text{kin}}$	$E_{\text{kin}}^{\text{DR}}$	$E_{\text{kin}}^{\text{MC}}$	$E_{\text{kin}}^{\text{fluc}}$	$E_{\text{mag}}$	$E_{\text{mag}}^{\text{tor}}$	$E_{\text{mag}}^{\text{pol}}$	$E_{\text{mag}}^{\text{fluc}}$
A1	4.428	1.152	0.015	3.261	0.876	0.050	0.055	0.771
<b>A2</b>	5.055	0.858	0.015	4.182	0.995	0.047	0.055	0.893
B	3.263	0.358	0.005	2.901	0.715	0.055	0.037	0.623
C1	3.153	0.164	0.003	2.986	0.504	0.035	0.026	0.442
C2	3.631	0.128	0.003	3.500	0.488	0.028	0.023	0.438
<b>C3</b>	6.572	3.941	0.003	2.628	0.891	0.177	0.023	0.692
D	3.181	0.873	0.003	2.305	0.671	0.042	0.012	0.617
E	4.189	2.317	0.001	1.871	0.579	0.073	0.023	0.483
F1	2.485	0.842	0.002	1.642	1.363	0.166	0.017	1.181
F2	2.898	1.101	0.002	1.794	1.082	0.088	0.023	0.971
F3	2.700	1.263	0.001	1.437	0.767	0.208	0.018	0.541
<b>G<sup>a</sup></b>	2.748	0.820	0.001	1.926	0.754	0.076	0.014	0.664
<b>G<sup>W</sup></b>	3.522	1.657	0.003	1.862	0.975	0.182	0.133	0.660
<b>H</b>	2.153	0.845	0.001	1.306	1.049	0.058	0.028	0.963
<b>H<sup>a</sup></b>	1.704	0.354	0.001	1.349	1.449	0.111	0.029	1.309
I	1.706	0.570	0.001	1.135	1.361	0.065	0.036	1.260
<b>I<sup>W</sup></b>	1.625	0.483	0.001	1.141	1.197	0.247	0.230	0.720
J	0.580	0.346	0.000	0.234	0.113	0.024	0.006	0.083
<b>J<sup>W</sup></b>	0.786	0.101	0.000	0.685	0.900	0.102	0.230	0.568
K1	2.325	1.624	0.000	0.701	0.426	0.216	0.025	0.185
K2	1.549	0.934	0.000	0.615	1.029	0.358	0.153	0.518
<b>L<sup>a</sup></b>	0.708	0.155	0.000	0.552	1.928	0.031	0.018	1.878
<b>L<sup>W</sup></b>	0.415	0.023	0.000	0.391	1.102	0.129	0.393	0.580
M	2.053	1.433	0.000	0.620	0.967	0.337	0.152	0.477
<b>M<sup>W</sup></b>	0.328	0.025	0.000	0.303	1.024	0.138	0.407	0.479

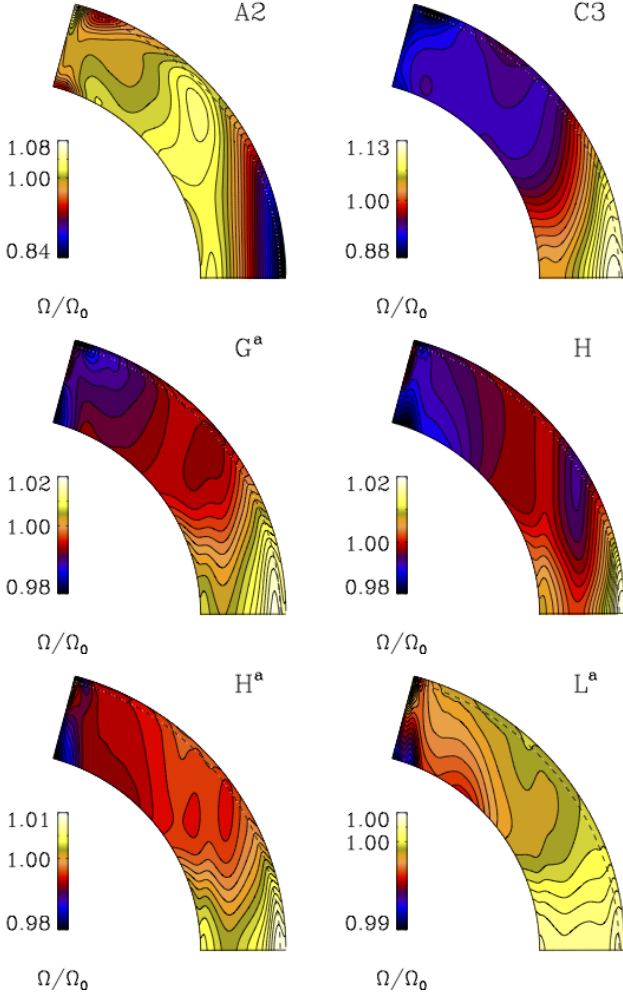


**Fig. 4.** Normalized angular velocity  $\Omega(r, \theta)$  of Runs A2, C3,  $G^a$ , H,  $H^a$ , and  $L^a$ . The dashed lines denote the radius  $r = 0.98R$ , which is used for the further analysis.

the nonaxisymmetric energy that also contains the fluctuations due to convective turbulence. Also the energies contained in differential rotation and meridional circulation show a decreasing overall trend as function of rotation. In general, the capability of the flow to extract energy from rotation is decreased by rotation. Comparison to wedge simulations indicates some differences on the dynamics of the flow, but it is hard to discern any systematic behavior. For moderate rotation Run G, the wedge version (Run  $G^w$ ) has an excess of every type of kinetic energy, while in the rapid rotation regime (Runs I, J, L, M) the kinetic energies have a tendency to be suppressed with respect to the full azimuth extent runs.

The rotation also influences the generation of mean flows as for example the differential rotation. To illustrate this, we plot the profiles of internal angular velocity,  $\Omega(r, \theta) = \bar{u}_\phi(r, \theta)/r \sin \theta$ , for six representative runs (Runs A2, C3,  $G^a$ , H,  $H^a$  and  $L^a$ ) in Fig. 4. We find anti-solar differential rotation for the solar rotation rate (Runs A1 and A2), which is consistent with many previous studies (e.g. Gastine et al. 2014; Käpylä et al. 2014) which might be due to the too high overall convective velocities or too high concentration of power at large spatial scales (Featherstone & Hindman 2016b) realized in the simulations in comparison to the Sun. The anti-solar rotation switches to solar-like at slightly more rapid rotation correspond-

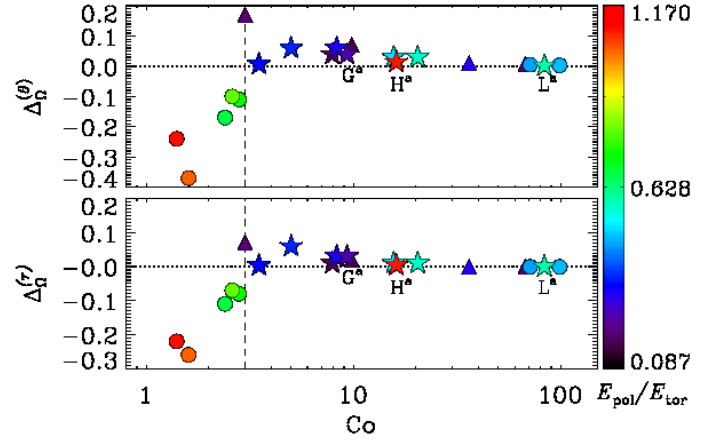


**Fig. 5.** Relative latitudinal differential rotation  $\Delta_\Omega^{(\theta)}$  (top panel) and relative radial differential rotation  $\Delta_\Omega^{(r)}$  (bottom panel) for all  $2\pi$  runs. The shape of the plotted symbols indicates the degree of nonaxisymmetry of the magnetic field (sphere - axisymmetric; triangle - mixed; star - nonaxisymmetric) while the color indicates the ratio of poloidal energy  $E_{\text{mag}}^{\text{pol}}$  to toroidal energy  $E_{\text{mag}}^{\text{tor}}$ , see Table 2. The dashed line ( $\text{Co} = 3$ ) indicates the transition from anti-solar to solar-like latitudinal differential rotation and the dotted lines indicate the zero. The high resolution runs  $G^a$ ,  $H^a$ , and  $L^a$  are marked for better visibility.

ing to  $\text{Co} = 3.0$ . For higher rotation rates the differential rotation develops a minimum at mid-latitudes. Such a configuration has been shown to be important in producing equatorward migrating magnetic activity (Warnecke et al. 2014). We find such minima also at moderate rotation, up to roughly seven times solar rotation rate (Run H). At higher rotation rates very little differential rotation is generated overall, and the mid-latitude minimum becomes progressively weaker.

We quantify the relative radial and latitudinal differential rotation using

$$\Delta_\Omega^{(r)} = \frac{\Omega_{\text{eq}} - \Omega_{\text{bot}}}{\Omega_{\text{eq}}}, \text{ and } \Delta_\Omega^{(\theta)} = \frac{\Omega_{\text{eq}} - \Omega_{\text{pole}}}{\Omega_{\text{eq}}}, \quad (19)$$

where  $\Omega_{\text{eq}} = \Omega(R, \pi/2)$  and  $\Omega_{\text{bot}} = \Omega(0.7R, \pi/2)$  are the angular velocities at the top and bottom of the convection zone at the equator, respectively, and  $\Omega_{\text{pole}} = [\Omega(R, \theta_0) + \Omega(R, \pi - \theta_0)]/2$  is the angular velocity at the latitudinal boundaries. Negative/positive values of  $\Delta_\Omega^{(\theta)}$  indicate anti-solar (fast pole, slow equator)/solar-like (fast equator, slow pole) differential rotation. In Table 1 we list these numbers from our simulations, and notice that a transition from strong anti-solar to significantly weaker solar-like differential rotation occurs at about  $\tilde{\Omega} \approx 1.8$  ( $\text{Co} \approx 3$ ; Run C3). We also plot  $\Delta_\Omega^{(r)}$  and  $\Delta_\Omega^{(\theta)}$  as functions of  $\text{Co}$  for all the  $2\pi$  runs in Fig. 5. There, we indicate the transition point with a vertical dashed line. As we will later discuss in detail, this point also marks the change of the dynamo modes from axisymmetric to nonaxisymmetric ones. From this plot it is evident that, as the rotation increases, both differential rotation measures approach zero. From Tables 1 and 2 we also see that near the transition, the rotation profile is sensitive to changes in the convective efficiency, that is described by the Rayleigh number. In Run C3, having a low  $\text{Pr}_{\text{SGS}}$ , and therefore lower Rayleigh and Reynolds numbers than in the more turbulent Runs C1 and C2, the rotation profile is solar-like while the others are convection anti-solar. This transition and its sensitivity to the efficiency

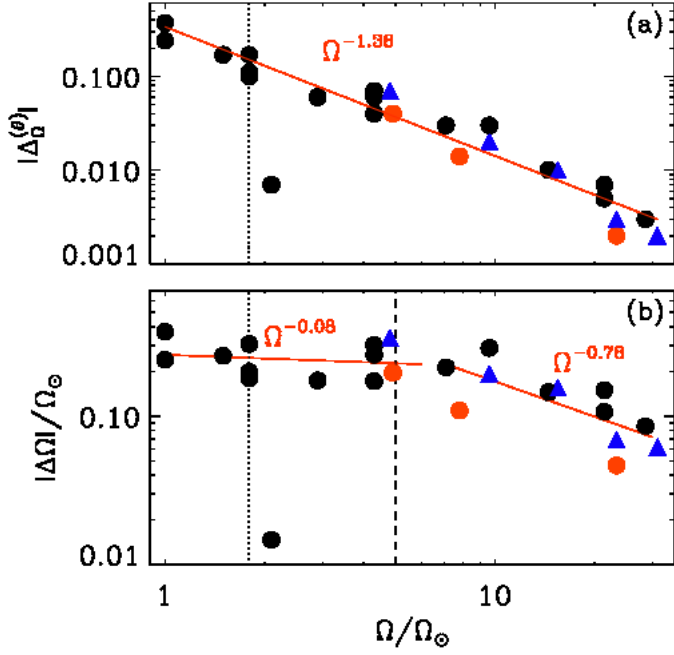


**Fig. 6.** Latitudinal differential rotation as a function of normalized rotation rate  $\Omega/\Omega_\odot$  showing the modulus of the relative differential rotation  $\Delta\Omega^{(\theta)}$  (a) and the modulus of the absolute differential rotation  $\Delta\Omega = \Delta\Omega^{(\theta)}\Omega_0$  normalized by the solar rotation rate (b). The red curves result from fitting. The black dashed line in panel b indicates the break in the slope. Red and black circles stand for high- and low-resolution  $2\pi$  runs, respectively, while blue triangles show the wedge runs. We note that for the fit in panel a and in panel b for moderate rotation, we do not take into account Run D with very low values.

of convection has been studied in detail by (e.g. Gastine et al. 2014; Käpylä et al. 2014).

Note that  $\Delta\Omega^{(r)}$  and  $\Delta\Omega^{(\theta)}$  measure only the difference between certain points and neglect the actual latitudinal variation, which can be more complicated. In the case of wedge geometry the flows near the latitudinal boundaries may not be representative of what takes place at high latitudes in real stars. These issues can lead to unrepresentative results in particular for the latitudinal differential rotation in cases where the latitudinal profile is non-monotonic (cf. Karak et al. 2015).

The anti-solar regime typically shows strong negative radial and latitudinal shear (Gastine et al. 2014), whereas magnetic fields tend to quench the differential rotation (e.g. Fan & Fang 2014; Karak et al. 2015). Our results are in agreement with those aforementioned studies. Another important aspect is the dependence of differential rotation on the rotation rate itself. Several numerical studies have shown that the relative differential rotation decreases significantly as a function of the rotation rate (e.g. Käpylä et al. 2011; Gastine et al. 2014). This is confirmed by our simulations; see Fig. 6a, where we plot  $\Delta\Omega^{(\theta)}$  as function of rotation rate. What sets our study apart from previous ones is that we probe significantly broader range of rotation rates. This allows us to search for power-law behavior of the relative differential rotation as a function of  $\tilde{\Omega}$  of the form  $\Delta\Omega^{(\theta)} \propto \Omega^q$ . We fit a slope of  $q = -1.38$ , close to observational studies that indicate values of  $q$  that are slightly below (e.g. Reinhold & Gizon 2015) or above unity (e.g. Lehtinen et al. 2016) and with mean-field

models based on analytic turbulence models (e.g. Kitchatinov & Rüdiger 1999). In this regime, the wedge and full azimuthal extent runs show a very similar trend independent of resolution.

For the absolute latitudinal differential rotation,  $\Delta\Omega = \Delta\Omega^{(\theta)}\Omega_0$ , Fig. 6b, we do not find, however, a single power-law that would describe the behavior at all rotation rates. For slow and moderate rotation, up to  $\tilde{\Omega} \approx 5$ , we fit a slope of  $-0.08$ , while for the highest rotation rates investigated,  $\tilde{\Omega} \approx 5 - 31$ , we find a steeper power-law of about  $-0.78$ . The behavior for slow and moderate rotation fits well with the theoretical and observational findings mentioned before, but the behavior for rapid rotation disagrees. This disagreement cannot be explained by the lack of supercriticality as the high-resolution runs show even lower differential rotation as their low-resolution counterparts. However, the magnetic fields in the rapidly rotating high-resolution runs ( $H^a$  and  $L^a$ ) are generally stronger than in the lower resolution ones, possibly explaining the reduced differential rotation (cf. Käpylä et al. 2017).

### 3.3. Overview of magnetic states

All the runs discussed in this work produce large-scale magnetic fields. Very similar wedge runs were recently analysed by Warnecke et al. (2017) using the test-field method, who measured significant turbulent effects contributing to the magnetic field generation. Therefore, we attribute the magnetic fields seen in the current runs to the turbulent dynamo mechanism. To describe the magnetic solutions, we first look at the volume-averaged magnetic energy densities. We define them analogously to their kinetic counterparts. We use

$$E_{\text{mag}} = \langle \mathbf{B}^2 \rangle_V / 2\mu_0, \quad (20)$$

for the total magnetic energy density,

$$E_{\text{mag}}^{\text{tor}} = \langle \overline{B}_\phi^2 \rangle_V / 2\mu_0, \quad E_{\text{mag}}^{\text{pol}} = \langle \overline{B}_r^2 + \overline{B}_\theta^2 \rangle_V / 2\mu_0, \quad (21)$$

for contribution of the mean toroidal and mean poloidal field and

$$E_{\text{mag}}^{\text{fluc}} = E_{\text{mag}} - (E_{\text{mag}}^{\text{tor}} + E_{\text{mag}}^{\text{pol}}) \quad (22)$$

for the contribution of fluctuating magnetic field. These quantities are listed in Table 2. We find that for all the runs the contributions from fluctuating magnetic field dominates the magnetic energy. The axisymmetric contributions contain on the order of 5 to 10 per cent of the total magnetic energy in the majority of the runs, and exceeds 15 per cent only in Runs C3, F3, K1, and K2. These runs are characterized either by a low  $\text{Pr}_{\text{SGS}}$  (C3 and F3) or rapid rotation (K1 and K2), both leading to reduced supercriticality of convection. Even though the contribution of the axisymmetric modes into the global energy balance seems to be rather low, already this manifests that there are large-scale flows and magnetic fields generated in the system.

In contrast to the kinetic energy, we do not find a clear trend for magnetic energies as a function of rotation rate. However, if we look at the radial profile of the magnetic energy density for a selection of runs (Fig. 7), we find that the magnetic field in the upper half of the convection zone increases with rotation. As discussed earlier, we observe a simultaneous, nearly monotonic, decrease of the kinetic energy as function of rotation. Therefore, the ratio between the magnetic and kinetic energies, which is a diagnostic for the dynamo efficiency, is actually steeply increasing as a function of rotation, as can be seen from Fig. 8. From this figure we see that in the low-resolution cases the dynamo is clearly less efficient in the rapid rotation regime in comparison



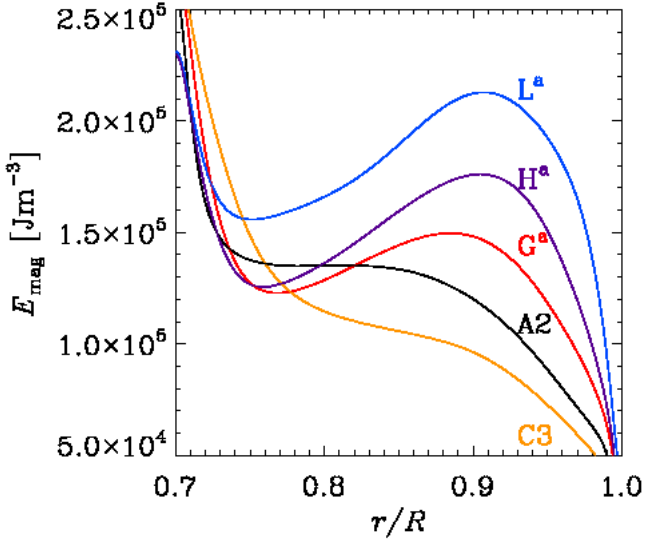


**Fig. 7.** Radial profiles of the total magnetic energy density  $E_{\text{mag}}$  averaged over time, latitude, and azimuth for Runs A2, C3,  $G^a$ ,  $H^a$ ,  $L^a$ .

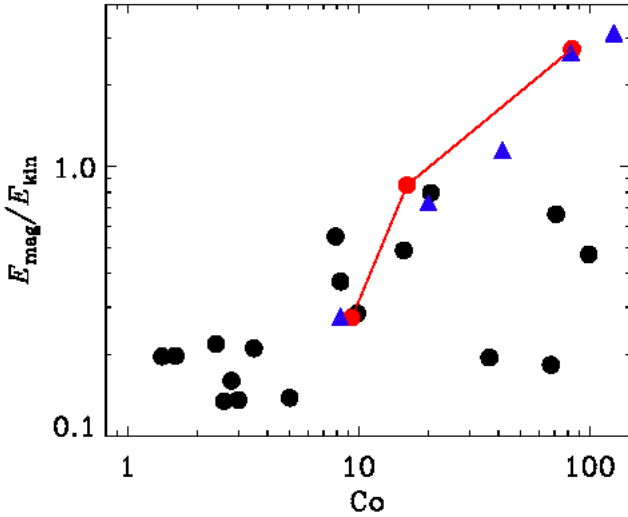


**Fig. 8.** Ratio of total magnetic to kinetic energies  $E_{\text{mag}}/E_{\text{kin}}$  as a function of Coriolis number  $Co$ . The red filled symbols (connected by a line) denotes high resolution runs. Blue triangles refer to wedge runs.

to the high-resolution cases. We also observe that the wedge runs produce a far more efficient dynamo in the rapid rotation regime than the corresponding low-resolution runs with full azimuthal extent. This is possibly explained by the somewhat higher stratification and Rayleigh numbers in the wedge runs in comparison to those in the low resolution full  $2\pi$  models. We can conclude that the convective efficiency directly influences the dynamo efficiency and therefore the magnetic energy production.

In Fig. 5 we study the dependence of the overall magnetic topology on the amount of differential rotation generated in the system. The ratio of poloidal to toroidal field energy, shown with the color of the symbols, is systematically changing from mostly poloidal field configurations at very low rotation rates into toroidal ones at moderate and rapid rotation. The energy

ratio gradually decreases, and with rotation rates exceeding the anti-solar to solar transition point, dominantly toroidal fields are seen. The strongest toroidal fields are generated for moderate rotation. At the highest rotation rates, the ratio of toroidal and poloidal becomes again lower. By inspecting Table 2, we notice that the wedge runs tend to produce a larger poloidal to toroidal ratio than the corresponding runs extending over the full azimuthal extent. The high-resolution cases (Runs  $H^a$  and  $L^a$ ) show more poloidal configurations, while the low-resolution cases do not show a systematic behavior.

We also depict the overall nonaxisymmetry of the large-scale magnetic field solutions with the shape of the symbol in Fig. 5. Again, on the lower rotation side of the break-point identified, the magnetic fields are mostly axisymmetric (circular symbol). On the rapid rotation side, the fields exhibit a significant non-axisymmetric component (triangles) and finally turn into completely nonaxisymmetric ones (stars). The resolution plays also a significant role for the nonaxisymmetry measure: the higher resolution runs show preferentially nonaxisymmetric configurations, while the lower-resolution runs turn back to axisymmetry at the highest rotation rates investigated.

To investigate the spatial structure of the magnetic field, we show snapshots of  $B_r$  of six representative runs in Fig. 9. At low rotation rates, most of the magnetic field is concentrated in the downflows between the convective cells, while at high rotation rates, the scale of convection, still clearly affecting the magnetic field thereby leaving a small-scale imprint on it, is significantly reduced. Nevertheless, global-scale magnetic field configurations clearly emerge at the high-latitude regions. It is immediately apparent that a nonaxisymmetric large-scale pattern is visible in all cases. In the slowly rotating cases the nonaxisymmetric component is sub-dominant, but the equatorial symmetry of it is clearly dipolar (antisymmetric with respect to the equator). In all runs with solar-like differential rotation, however, the field configuration is observed to be symmetric (or quadrupolar) with respect to the equator.

### 3.4. Degree of nonaxisymmetry

Large-scale nonaxisymmetric magnetic fields as seen in Fig. 9 are included in the definition of  $E_{\text{mag}}^{\text{fluc}}$  in Table 2, as this quantity is the difference between total and azimuthally averaged (mean) magnetic energies. This term contains, therefore, both small-scale fluctuations and actual large-scale nonaxisymmetric energy, and the diagnostics introduced so far describe the large-scale fields in the system only roughly.

In order to obtain a more complete picture, we perform a spherical harmonics decomposition of the radial components of the vector fields over constant radius slices at  $r = 0.98R$  with the method described in Sect. 2.3. The  $m = 0$  mode contains the axisymmetric (mean) part of the radial magnetic field,  $m = 1$  is the first nonaxisymmetric mode,  $m = 2$  the second, and so on. For the azimuthal  $\pi/2$  wedges, the first nonaxisymmetric mode is  $m = 4$ . The results of the decomposition are listed in Table 3.

We illustrate the quality of the reconstruction in Fig. 10 showing the radial magnetic field from Run  $L^a$  using different numbers of spherical harmonics. In the top panel, the reconstruction was obtained using  $1 \leq \ell \leq 10$ , while in the middle panel, the reconstruction is obtained summing over the first 100 spherical harmonics. The lowest panel shows the original data slice. We show a typical time series of different  $m$ -mode energies from the surface radial magnetic field reconstruction of Run  $H^a$  in Fig. 11. This run is dominated by the  $m = 1$  mode, which also shows cyclic variations over time, and also long-term changes,

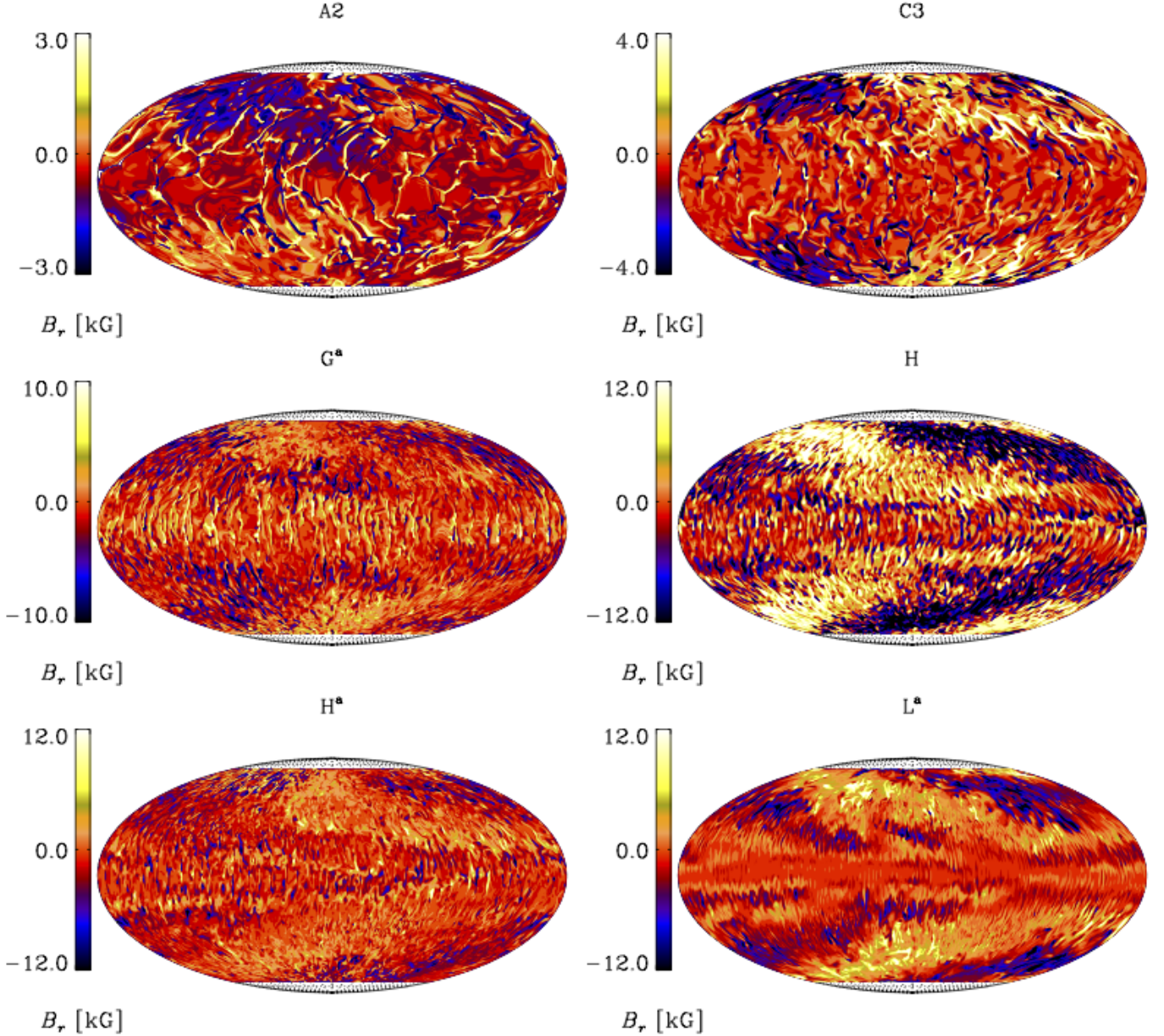


**Fig. 9.** Radial magnetic field  $B_r$  at  $r = 0.98R_\odot$  from the same runs as in Fig. 1.

during which the axisymmetric modes become comparable to the dominant mode for a short period of time.

The distribution of the radial magnetic energy density near the surface of the star is presented in Fig. 12a as a function of  $Co$ . Here we show the axisymmetric and the magnetic energy in the large-scale nonaxisymmetric field ( $1 \leq \ell \leq 5$ ), normalized to the total magnetic energy. We find an inversion between the energies in the axisymmetric and nonaxisymmetric components that corresponds also to the transition between anti-solar and solar-like differential rotation around  $Co \approx 3$ . The runs show a nonaxisymmetric magnetic field until  $Co \approx 70$ , where a bifurcation occurs: high-resolution runs remain nonaxisymmetric while low-resolution runs return to an axisymmetric configuration, indicating that high resolution is needed at such high rotation to capture the small scales. This could explain the lack of nonaxisymmetric solutions in the study of Brown et al. (2010). This conjecture is supported by the fact that in the higher resolution simulations of Nelson et al. (2013) significantly clearer non-

axisymmetric features are seen (their Figs. 4–6), although they are confined at low latitudes. These simulations were made with  $\tilde{\Omega} = 3\Omega_\odot$ , albeit with a lower thermal Prandtl number, and different viscosity and diffusivity profiles than those in the current simulations (cf. Appendix A of Käpylä et al. 2017). However, our Runs C3 and F3 also produce strong nonaxisymmetric large-scale fields also at high latitudes despite their lower values of  $Pr_{SGS}$ . This could be an indication of the influence of the latitudinal boundaries present in the current simulations.

The simulations of Fan & Fang (2014) and Hotta et al. (2016), on the other hand, used the solar rotation rate and a further enhanced thermal Prandtl number to force a solar-like rotation profile. The large-scale magnetic fields in these simulations are characterized by dominant low-latitude axisymmetric fields which show apparently random polarity reversals. The results of these studies are most closely related to our slowly rotating Runs A1, A2, and B which also produce predominantly axisymmetric large-scale fields, although with anti-solar differ-

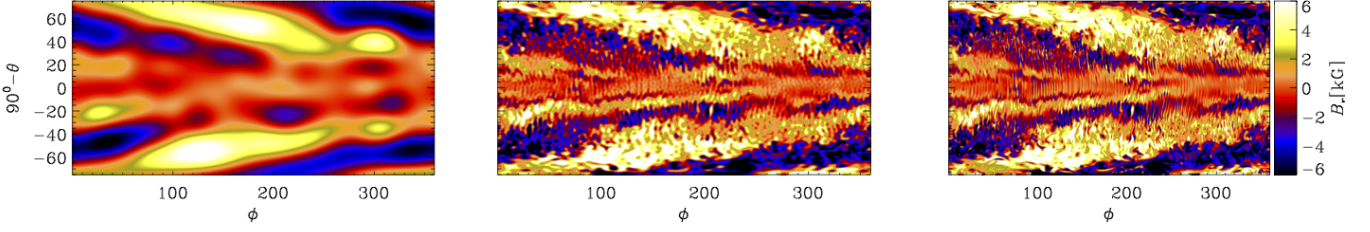


**Fig. 10.** Spherical harmonic reconstruction, using  $1 \leq \ell \leq 10$  harmonics (left panel) and  $1 \leq \ell \leq 100$  harmonics (middle panel), and original of the radial magnetic field (right panel) near the surface ( $r = 0.98R$ ) of Run  $L^a$ .

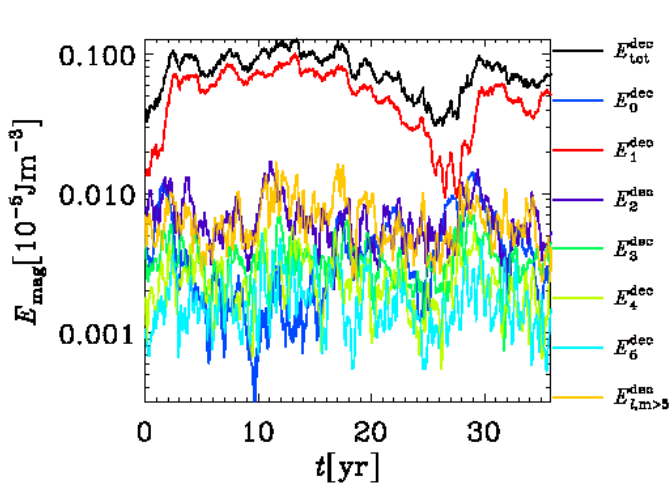


**Fig. 11.** Time series of the total radial magnetic energy from decomposition (in black) and each of the  $m$  modes. Blue:  $m = 0$ , red:  $m = 1$ , violet:  $m = 2$ , light green:  $m = 3$ , olive green:  $m = 4$ , light blue:  $m = 5$ , orange: small-scale magnetic fields. The modes from  $m = 3$  on are smoothed over five neighboring points in time.

ential rotation. This seems to suggest that axisymmetric fields are preferred at slow rotation irrespective of the differential rotation profile.

From Table 3 we notice that  $m = 1$  is the first large-scale nonaxisymmetric mode excited as the rotation increases. Some higher  $m$ -modes get excited, too, but they remain, on average, subdominant to the first nonaxisymmetric mode, and therefore the runs are well described by these two modes, shown in Fig. 12b. The axisymmetric energy is dominant at low rotation,  $Co \leq 3$ , which is also the separation between anti-solar and solar-like differential rotation. In the range  $3 \leq Co \leq 72$  the first nonaxisymmetric mode is dominant, but its strength decreases for the low resolution runs for  $Co > 20$ , and eventually there is a return to an axisymmetric configuration at the highest values of  $Co$ . For the high-resolution runs, however, the  $m = 1$  mode energy keeps increasing until the highest rotation rates investigated.

### 3.5. Magnetic cycles and dynamo waves

In all runs we see some time variation in the magnetic energy. In the Runs A1, A2, and B, all with anti-solar differential rotation profiles, we do not see much time dependence in the time-latitude (butterfly) diagrams of the mean toroidal magnetic fields; see the upper left panel of Fig. 13 for an example from Run A2. The time evolution of the magnetic energy

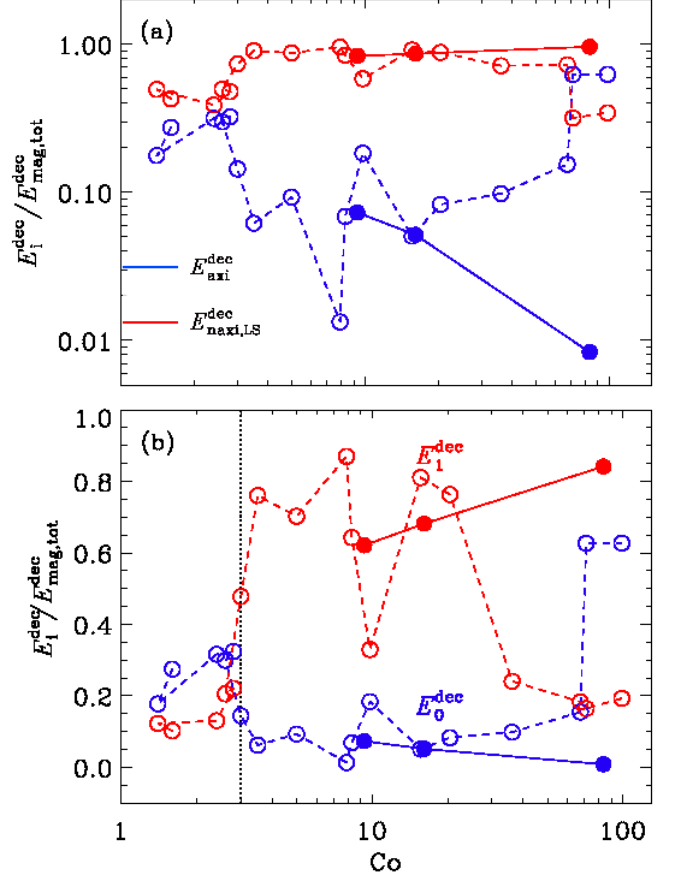


**Fig. 12.** Axisymmetric mean ( $m = 0$ , blue) energy versus non-axisymmetric large-scale ( $m = 1, 5$ ; red) energy fraction at the surface (a). Axisymmetric mean ( $m = 0$ ; blue) energy fraction versus the first nonaxisymmetric mode ( $m = 1$ ; red) energy fraction (b). The dotted black line denotes the axisymmetric to nonaxisymmetric transition at region  $Co \approx 3$ . In both plots, the dashed red and blue lines connect  $2\pi$  runs, filled symbols, connected with solid lines, denote the high resolution runs.

in these runs cannot be described as periodic, but still we see cyclic variation around a mean level, albeit with a poorly defined cycle length. By counting how many times the mean level is crossed, sometimes referred to as the syntactic method (Chen 1988, Chapter 9.4), we can assign these runs a characteristic time scale of change,  $\tau_{cyc}$ . Even though the other runs show much clearer cyclic time variability, for consistency, this approach is used to determine the cycle periods even for these runs. Starting from Runs C1, C2, and C3 onwards to higher rotation rates (other panels of Fig. 13), however, more systematic patterns are discerned in the time series and butterfly diagrams. Runs C1 and



**Table 3.** Energy densities of the radial magnetic field decomposition into spherical harmonics near the surface ( $r = 0.98R$ ) in units of  $10^5 \text{J m}^{-3}$  and dynamo cycle properties.

Run	$E_{\text{mag}}^{\text{surf}}$	$E_{\text{mag,tot}}^{\text{dec}}$	$E_0^{\text{dec}}$	$E_1^{\text{dec}}$	$E_2^{\text{dec}}$	$E_3^{\text{dec}}$	$E_4^{\text{dec}}$	$E_5^{\text{dec}}$	$E_{l,m>5}^{\text{dec}}$	$P_{\text{ADW}}[\text{yr}]$	$P_{\text{ADW}}/P_0$	$P_{\text{ADW}}/P_{\text{DR}}$	$D$	$\tau_{\text{cyc}}[\text{yr}]$
A1	0.211	0.021	0.006	0.002	0.002	0.002	0.002	0.001	0.006					3.72 <sub>(m0)</sub>
A2	0.188	0.024	0.004	0.003	0.002	0.002	0.002	0.002	0.008					4.13 <sub>(m0)</sub>
B	0.183	0.023	0.007	0.003	0.002	0.002	0.001	0.001	0.007					2.45 <sub>(m0)</sub>
C1	0.137	0.017	0.006	0.004	0.001	0.001	0.001	0.001	0.003					3.53 <sub>(m0)</sub>
C2	0.128	0.016	0.005	0.003	0.001	0.001	0.001	0.001	0.003					4.37 <sub>(m0)</sub>
<u>C3</u>	0.142	0.024	0.003	0.012	0.002	0.002	0.001	0.001	0.003	19.53	474	44.83	R	3.13 <sub>(m0)</sub>
D	0.180	0.051	0.003	0.039	0.003	0.002	0.001	0.002	0.002	14.14	410	24.67	R	18.25 <sub>(m0)</sub>
E	0.147	0.031	0.003	0.021	0.002	0.001	0.001	0.001	0.001	39.87	1542	82.53	R	10.31 <sub>(m1)</sub>
F1	0.290	0.111	0.001	0.097	0.005	0.002	0.001	0.001	0.003	4.22	245	5.92	R	6.68 <sub>(m0)</sub>
F2	0.220	0.049	0.003	0.031	0.004	0.002	0.002	0.001	0.004	5.94	346	6.55	R	8.05 <sub>(m1)</sub>
F3	0.086	0.016	0.003	0.005	0.001	0.001	0.001	0.001	0.004	10.49	611	8.20	R	5.74 <sub>(m0)</sub>
<u>G<sup>a</sup></u>	0.254	0.055	0.004	0.034	0.005	0.003	0.002	0.001	0.005	8.93	583	8.60	R	7.43 <sub>(m1)</sub>
<u>G<sup>W</sup></u>	0.285	0.039	0.029	0.000	0.000	0.000	0.007	0.000	0.003					2.37 <sub>(m0)</sub>
H	0.053	0.022	0.001	0.018	0.001	0.000	0.000	0.000	0.001	42.69	1916	12.15	R	27.34 <sub>(m1)</sub>
<u>H<sup>a</sup></u>	0.274	0.077	0.004	0.053	0.007	0.003	0.002	0.002	0.006	24.36	2560	15.84	R	7.17 <sub>(m1)</sub>
I	0.274	0.107	0.009	0.082	0.006	0.003	0.002	0.001	0.004	11.66	1522	7.07	R	7.75 <sub>(m1)</sub>
<u>I<sup>W</sup></u>	0.220	0.040	0.030	0.000	0.000	0.000	0.008	0.000	0.003					4.44 <sub>(m0)</sub>
J	0.014	0.0020	0.0002	0.0005	0.0004	0.0003	0.0002	0.0001	0.0004	5968	535724	382.59	SW, P	8.25 <sub>(m0)</sub>
<u>J<sup>W</sup></u>	0.421	0.129	0.072	0.000	0.000	0.000	0.046	0.000	0.011					4.05 <sub>(m0)</sub>
K1	0.025	0.004	0.001	0.001	0.001	0.001	0.0002	0.0001	0.0004	4.89	1418	0.01	P	1.24 <sub>(m0)</sub>
K2	0.193	0.059	0.037	0.010	0.004	0.002	0.002	0.001	0.003					5.10 <sub>(m0)</sub>
<u>L<sup>a</sup></u>	0.475	0.292	0.002	0.246	0.013	0.012	0.006	0.004	0.008	56.53	17821	14.66	SW, R	3.13 <sub>(m1)</sub>
<u>L<sup>W</sup></u>	0.509	0.218	0.123	0.000	0.000	0.000	0.081	0.000	0.013					5.68 <sub>(m0)</sub>
<u>M</u>	0.133	0.049	0.030	0.009	0.003	0.002	0.001	0.001	0.001					6.64 <sub>(m0)</sub>
<u>M<sup>W</sup></u>	0.462	0.197	0.135	0.000	0.000	0.000	0.051	0.000	0.011					4.10 <sub>(m0)</sub>

**Notes.** Here  $E_{\text{mag}}^{\text{surf}}$  is the total energy density,  $E_{\text{mag,tot}}^{\text{dec}} = \langle \mathbf{B}^2 \rangle_{\theta\phi t} / 2\mu_0$  is the magnetic energy density obtained from the decomposition over the first 10 harmonics, while  $E_m^{\text{dec}}$  denote the magnetic energy densities for the corresponding azimuthal wavenumbers with  $m = 0, \dots, 5$ , and  $E_{l,m>5}^{\text{dec}}$  the magnetic energy density in scales that are considered to be small-scale ( $m > 5$ ). The azimuthal dynamo wave rotation period  $P_{\text{ADW}}$  is computed as the latitudinal and temporal average of the maximum phase of the dynamo mode. The ratio  $P_{\text{ADW}}/P_0$  indicates the average period of the ADW compared to the bulk rotation ( $P_0 = 2\pi/\Omega_0$ ). The ratio  $P_{\text{ADW}}/P_{\text{DR}}$  indicates the average period of the ADW compared to the period of the differential rotation.  $D$  indicates if the ADW is moving in the retrograde (R) or prograde (P) direction. SW indicates a standing wave. Furthermore,  $\tau_{\text{cyc}}$  is the characteristic timescale of the change related to the dominant dynamo mode, which is indicated in the parenthesis. If the solution exhibits oscillatory behavior, the run label is underlined.

C2 present two very interesting cases, as it is very rare to obtain cyclic dynamo solutions in the regime of anti-solar rotation profiles, which these runs clearly posses. Furthermore, it is clear that simulations with a  $2\pi$  azimuthal extent are capable of producing oscillating dynamo solutions at lower rotation rates than corresponding runs in wedges.

The last column in Table 3 shows the characteristic time associated with the evolution of the dominant dynamo mode from the surface energies,  $\tau_{\text{cyc}}$ , independent of whether or not the time variation is linked to corresponding variability in the butterfly diagram or equivalent. We judge that this more closely corresponds to the observational situation, where for the majority of cases only the light curve variability is seen while the surface magnetic field evolution is hidden. In order to calculate it, we consider the time variation of the dominant modes ( $m = 0$  and  $m = 1$ ) and count how many times they oscillate around their mean value. The mode considered for the time variation is listed as a subscript. For the runs where they have comparable strength, we observed that  $\tau_{\text{cyc}}$  does not vary irrespective of which of the two modes is used. In such a case we chose  $m = 0$ .

After estimating the characteristic time, we can determine the activity cycle period,  $P_{\text{cyc}} = \tau_{\text{cyc}}$ , see how it varies with rotation, and compare with some observational results (Saar &

Brandenburg 1999; Lehtinen et al. 2016). We show the results in Fig. 14a where we plot the ratio between rotation and activity period against the Coriolis number. We see that the transition line  $\text{Co} = 3$  divides the runs into two populations: one where the anti-solar axisymmetric models cluster and another where the solar-like non-axisymmetric models cluster. The former population is centered to the upper left corner of the plot, and appears to form what is referred to as the inactive branch in Brandenburg et al. (1998); Saar & Brandenburg (1999). The latter population, shown in red, falls on a clearly separate branch that has a negative slope. The simulation data coincides with a slope  $\text{Co}^{-0.43}$  determined by Saar & Brandenburg (1999) for the superactive (S) branch. However, we cannot clearly identify an active (A) branch nor the transition in between the A and S branches that are clearly present in Saar & Brandenburg (1999). The dashed vertical line denotes the observational transition of stars without active longitudes to ones with them in a sample of solar-like rapid rotators (Lehtinen et al. 2016). We note that in our simulations active longitudes occur for considerably lower Coriolis numbers ( $\text{Co} > 3$ , corresponding to the leftmost dotted line).

The best available measure of the magnetic activity from our simulations is the ratio of the magnetic to kinetic energy, that can be directly thought to measure the efficiency of the

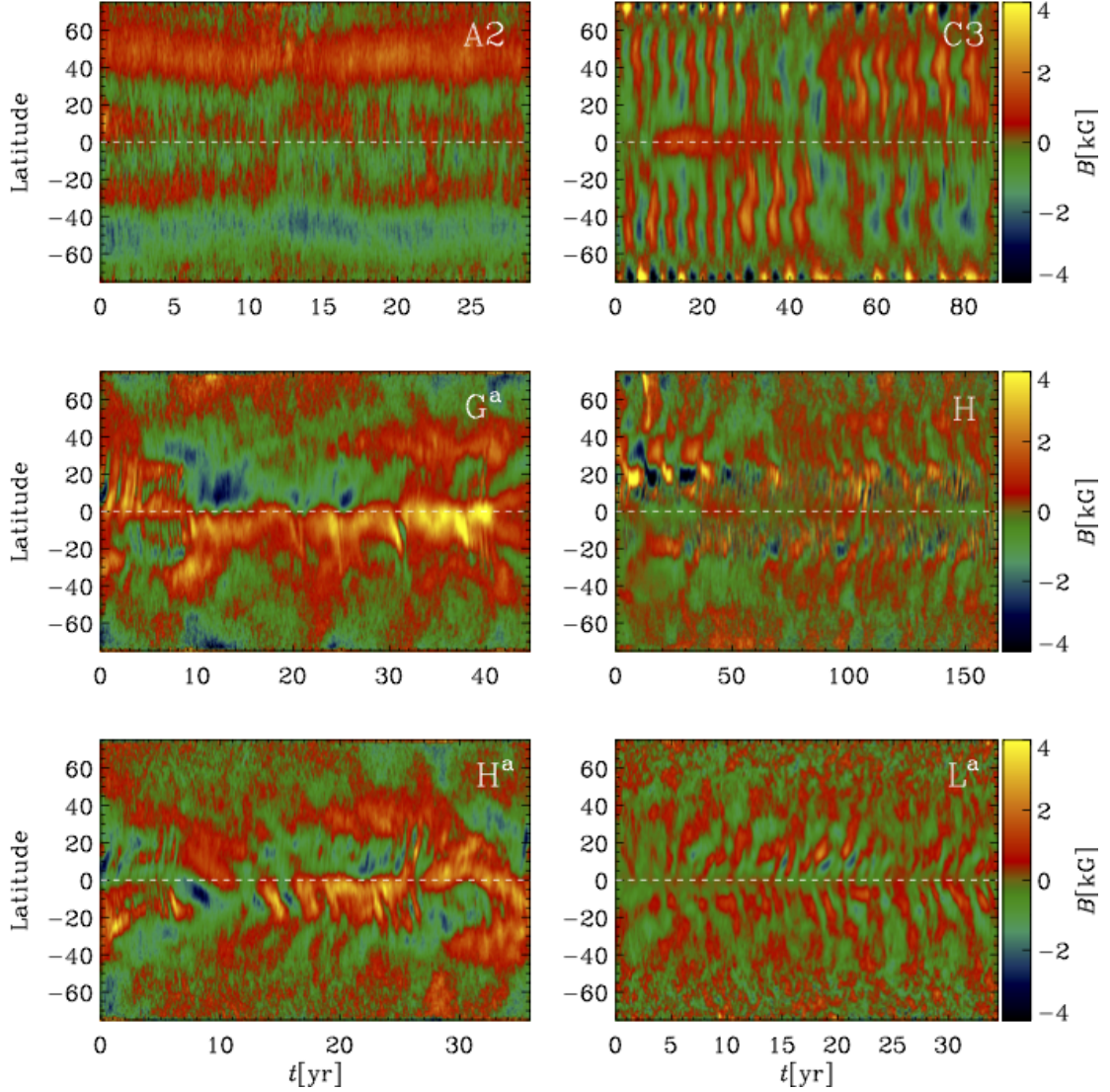


**Fig. 13.** Mean toroidal magnetic field  $\overline{B}_\phi$  from Runs A2 (top left), C3 (top right),  $G^a$  (middle left), H (middle right),  $H^a$  (bottom left), and  $L^a$  (bottom right) shown near the surface  $r = 0.98R$ .

dynamo, see Fig. 8. Figure 14b shows the rotation-activity period ratio as a function of this quantity. In this plot, the inactive branch is separated even more clearly from the active-superactive branch, having a clearly positive slope. The active-superactive branch still remains inseparable, but the population of simulations falling on this branch still shows a distinct, negative slope. Our results show a much more versatile behavior than those of Strugarek et al. (2017), where only a limited range of rotation rates were examined. In their study, only the behavior on the inactive branching was qualitatively captured, while in our study we start capturing the behavior in the active/superactive branches.

In some cases we find an equatorward migrating oscillatory magnetic field in the initial stages of the simulation (for example, Runs G and H), see Fig. 13. Later, however, the dominant dynamo mode changes to a nonaxisymmetric one soon after the large-scale field reaches dynamically significant strengths. This behavior has been found in Käpylä et al. (2013), where the wedge and the  $2\pi$  version of Run F1 has been compared. Thus, we conclude that the wedge geometry significantly changes the behavior of the dynamo by suppressing the large-scale nonax-

isymmetric modes ( $m = 1, 2, 3$ ). Also, we observe that for cyclic solutions to emerge in wedges, we require a generally higher Coriolis number than in runs with full azimuthal extents.

Time variations are seen also in the cases of nearly purely nonaxisymmetric solutions, one such example being the high-resolution Run  $L^a$ . The magnetic field in this run forms two active longitudes that remain fixed on the stellar surface, having opposite polarities in each hemisphere, but exhibiting a quadrupolar symmetry with respect to the equator. The weak axisymmetric component also exhibits time variability, as can be seen from the butterfly diagram plotted in Fig. 13. Both the axi- and nonaxisymmetric components develop time variability over a similar time scale of roughly 3 years. The active longitude strengths are modulated in this time scale in such a way that the ones in the other hemisphere grow simultaneously, while the ones on the other decay, followed by a reversed behavior, see Fig. 15. However, no clear polarity reversals are related to this time variation. In other words, we observe that maximum and minimum on the same hemisphere never switch in intensity, as is happening in the flip-flop phenomenon (Hackman et al. 2013; Berdyugina & Tuominen 1998).



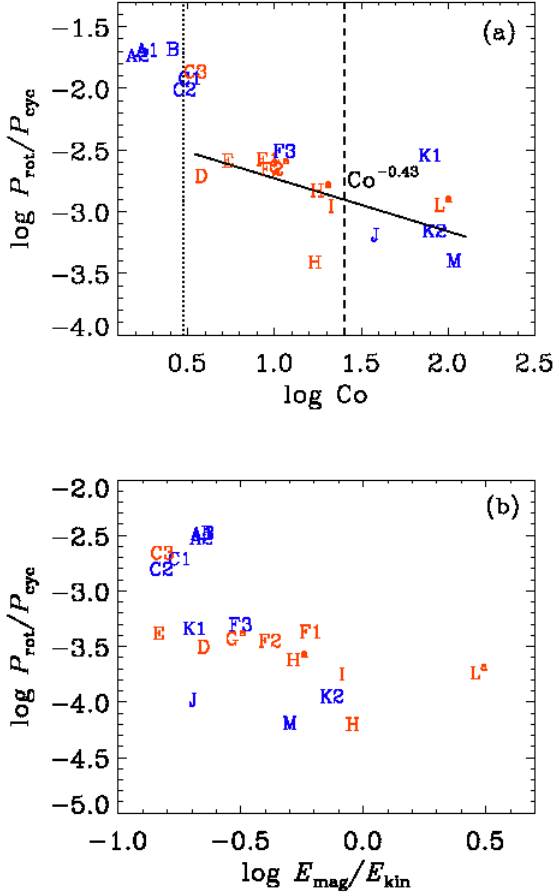


**Fig. 14.** Ratio of the rotation period to the cycle period as a function of Coriolis number in logarithmic scale (a). The dashed line is the same as the one in Lehtinen et al. (2016). The black line with slope  $\text{Co}^{-0.43}$  is the fit to the superactive (S) branch in Saar & Brandenburg (1999). The dotted line denotes the nonaxisymmetric transition ( $\text{Co} \geq 3$ ). Runs are plotted after their labels. The color indicates the mode chosen for calculating  $\tau_{\text{cyc}}$ : blue for  $m = 0$ , red for  $m = 1$ .  $P_{\text{rot}}/P_{\text{cyc}}$  as function of activity, represented by  $E_{\text{mag}}/E_{\text{kin}}$  is shown in panel b.

To see whether flip-flops can occur in systems where there is a competition in between the  $m = 0$  and 1 modes, we analyze Run  $G^a$  in detail. As will be discussed later, this run exhibits an azimuthal dynamo wave that is migrating to the retrograde direction, and to better see the time evolution of the active longitudes, this migration has to be removed, as done in Fig. 16, lower panel. However, as in the case of  $L^a$ , the active longitudes are not switching in intensity between maxima and minima. In Run J, producing only a very weak dynamo solution with almost a standing azimuthal dynamo wave, a polarity change can, however, be detected, as is depicted in Fig. 16, upper panel. The active longitudes are seen to stay nearly fixed in the orbital frame of reference, and after quasi-regular time points, the polarity of both reverses quite abruptly. In this case the magnetic field is clearly sub-dominant with respect to the velocity field, but nevertheless the advection by the differential rotation explains very poorly the time evolution of the active longitudes.

Another phenomenon that has recently been related to active longitudes from models (Cole et al. 2016) and also observations (see e.g. Lindborg et al. 2013) is the so-called azimuthal

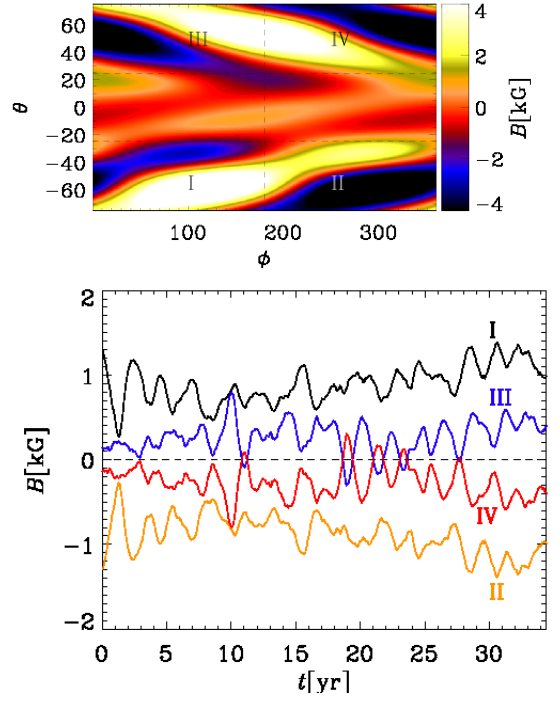


**Fig. 15.** Standing dynamo wave of Run  $L^a$ . The lower panel shows the time variation of the four regions indicated in the upper plot.

dynamo wave (ADW). This term refers to active longitude systems which migrate in the orbital reference frame of the star. A useful comparison is the latitudinal dynamo wave visible in the Sun: this dynamo wave shows a dependence in latitude, visible as the appearance of sunspots at lower latitudes as the solar cycle progresses, but the spots do not appear with a preferential location in longitude. On the contrary, the ADW has no dependence in latitude, but it is shifted in longitude and time or appears as a standing wave. The migration direction has been observed to be preferentially prograde (see e.g. Berdyugina & Tuominen 1998; Lindborg et al. 2013; Lehtinen et al. 2016), but also a standing wave for  $\sigma$  Gem and a retrograde wave for EI Eri have been reported (Berdyugina & Tuominen 1998).

Next, we search for an azimuthal dynamo wave in the runs with a significant  $m = 1$  mode. The results for the reconstruction of the first nonaxisymmetric mode of the radial magnetic field as functions of time and longitude for Runs C3,  $G^a$ ,  $H^a$ , and  $L^a$  are shown in Fig. 17 for  $60^\circ$  northern latitude. In all the runs presented here, the  $m = 1$  mode is rigidly rotating and has a different pattern speed than the gas. To verify that the magnetic field is detached from the flow, we plot the expected advection due to differential rotation at the same latitude and compare the results at different latitudes. If the magnetic field was advected by the mean flow, then its maxima and minima would fall on the black and white lines representing the surface differential rotation. In the range  $3 \leq \text{Co} \leq 68$ , we always observe that the magnetic field is following a pattern different from the differential rotation at the surface of the star.

The parameters related to the ADW are listed in columns 11–15 of Table 3. The period of the ADW,  $P_{\text{ADW}}$ , is calculated as the first derivative with respect to time of the maximum of the phase of the  $m = 1$  mode. We compare it with the bulk rotation,  $P_{\text{ADW}}/P_0$ , and the differential rotation,  $P_{\text{ADW}}/P_{\text{DR}}$ , where  $P_0 = 2\pi/\Omega_0$  and  $P_{\text{DR}} = 2\pi/(\langle\Omega - \Omega_0\rangle(r = 0.98R))_\theta$  respectively, and indicate the direction of the wave, retrograde

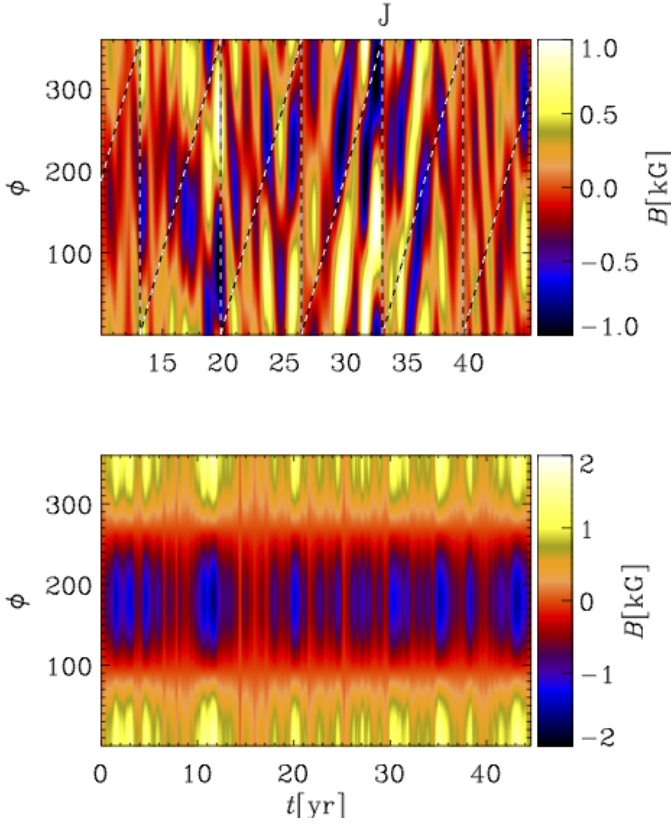


**Fig. 16.** *Upper panel:* flip-flop for Run J. *Lower panel:* same picture as in Fig. 17 for Run  $G^a$ . The ADW has been de-migrated to show the active longitudes.

(R, westward) or prograde (P, eastward) in the column marked  $D$ . A retrograde wave is a wave moving in the opposite direction with respect to the bulk rotation. Its period, therefore will be larger than the rotation period. On the other hand, a wave moving in the prograde direction will have a shorter period. In most of our cases, we find retrograde ADWs, and only in three cases (Runs J, K1,  $L^a$ ) the behavior is different. Runs J and K1 are characterized by rapid rotation and a low value of magnetic energy and the azimuthal dynamo wave has a smaller amplitude than in the other cases. In Runs  $L^a$  and J the dynamo wave is drifting very slowly<sup>2</sup>. Over the time scale of which the runs are integrated, these represent standing waves rather than migratory phenomena (therefore identifier SW in Table 3). Their almost insignificant migrations occur in opposite directions with Run J showing prograde migration. In the parameter regime included in this study the retrograde migration is clearly the dominant one. The magnetic cycle seems not to be related in any way to migration period of the ADW.

#### 4. Conclusions

In this paper, we have performed an extensive study of the effect of rotation rate on convection-driven spherical dynamos, covering a range from 1 to 31 times the solar value,  $\Omega_\odot$ , corresponding to  $Co = 1.6$  to 127. The dependence of stellar dynamos on rotation speed has been assessed over a range that is much wider than what has been studied previously. For example, Strugarek et al. (2017) studied the change of cycle frequency

<sup>2</sup> A video of the surface radial magnetic field evolution of Run  $L^a$  can be found from <https://www.youtube.com/watch?v=2g4r1uanrj4>

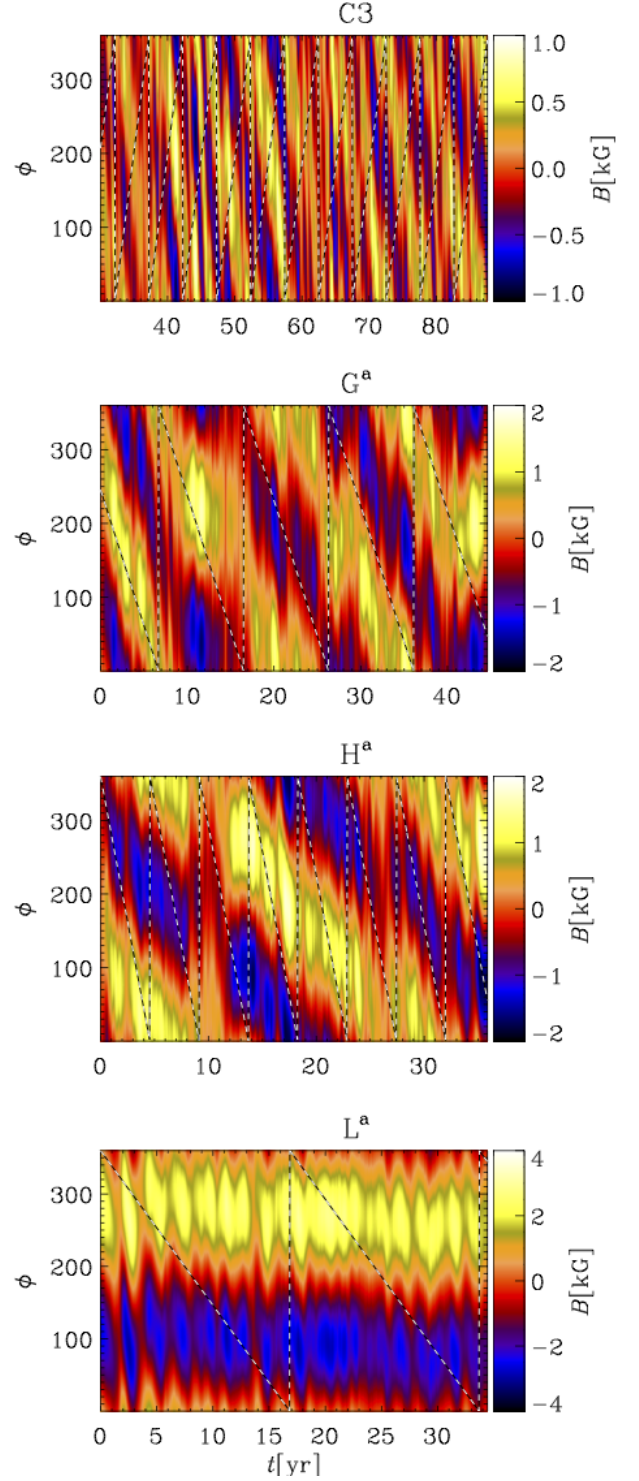


**Fig. 17.** Reconstruction of the  $m = 1$  mode of the magnetic field at the surface of the star for Runs C3,  $G^a$ ,  $H^a$ , and  $L^a$  at  $\theta = +60^\circ$ . The black and white line is the path due only to differential rotation.

while changing the rotation rate by a factor of two, resulting in a change in  $Co$  of about a factor of three. We found that, for  $\Omega \gtrsim 1.8\Omega_\odot$  ( $Co \gtrsim 3$ ), nonaxisymmetric modes are excited and azimuthal dynamo waves are present. The most commonly excited configuration in our models is the  $m = 1$  mode accompanied with an  $m = 0$  mode comparable (for moderate rotation) or sub-dominant (for rapid rotation) in strength. The magnetic field

near the surface is symmetric (quadrupolar) with respect to the equator in all cases with an anti-solar differential rotation profile. The axisymmetric part of the magnetic field is more toroidal at moderate rotation, while preferentially more poloidal configurations are indicated from the the highest rotation rates studied. In the slow rotation regime with anti-solar differential rotation, the solutions are preferentially axisymmetric and poloidal. The same pattern over the azimuthal direction can be seen observationally in the distribution of active longitudes or the magnetic field geometries of stars with different rotation rates. Lehtinen et al. (2016) found from time series photometry of active solar-type stars that there is an onset of active longitudes at around  $Co \approx 25$ . Similarly, surface magnetic field mapping using ZDI has shown that solar-type stars have a transition between axisymmetric poloidal and nonaxisymmetric toroidal field geometries at around  $Co \approx 13$  (or  $Ro = P_{rot}/\tau_c \approx 1$ ; Donati & Landstreet 2009; See et al. 2016), where  $\tau_c$  is the convective turnover time. This split is not absolute and the rapidly rotating stars can still alternate between toroidal and poloidal fields (Kochukhov et al. 2013). Moreover, Rosén et al. (2016) observed that for rapid rotators the degree of nonaxisymmetry tends to increase towards more poloidal field geometries. This may indicate a similar behavior as in the high resolution models which develop nonaxisymmetric poloidal fields at the highest rotation rates. We note here that the toroidal and poloidal field is computed differently from observations, namely from the total surface field, than here, namely computing it only for the axisymmetric mean field of the whole convection zone.

The different values for the axisymmetric to nonaxisymmetric transition may be due to several factors. Firstly, the criteria for detecting nonaxisymmetric structures may not be fully comparable between the different studies. Secondly, the observational studies use semi-empirical values of the convective turnover time  $\tau_c$  while in this study we have used the definition  $\tau_c = 2\pi u_{rms}/0.3R$ . Lastly, it is worth noting that the simulations do not occupy the same exact parameter space as real stars. Furthermore, a different value of  $Co$  could just be explained by a different depth in the star where the dynamo is mainly driven, as  $u_{rms}$  has a strong radial dependency. The observations do not show any indication that the most rapidly rotating stars would turn again to having axisymmetric fields, as is the case with the low resolution runs in this study. The bifurcation of the fast rotating low resolution runs turning back to axisymmetric fields and high resolution runs remaining nonaxisymmetric may simply be a symptom of inadequate convective efficiency and insufficient capturing of small-scales in the low resolution runs.

In our set of runs, we found mostly retrograde azimuthal dynamo waves, in contrast with observations of solar-like stars that show a preference for prograde direction (Lehtinen et al. 2016). The prograde pattern speeds may be analogous to those seen in the Sun. Its supergranulation pattern is found to rotate a few percent faster than the gas at the surface (Gizon et al. 2003). Similarly, magnetic tracers including sunspots are seen to rotate faster than the gas (Pulkkinen & Tuominen 1998). The occurrence of prograde pattern speeds is theoretically associated with the near-surface shear layer of the Sun (Green & Kosovichev 2006; Busse 2007; Brandenburg 2007). Thus, a reason for this discrepancy could be the fact that we simulate only the stellar convection zone and we do not include the near surface shear layer, which should lead to a prograde directed wave.

In the interval  $1-1.8\Omega_\odot$ , corresponding to  $Co = 1.6-2.8$ , we find anti-solar differential rotation, in agreement with previous studies, such as Käpylä et al. (2014) and Gastine et al. (2014). We do not see any oscillatory behavior of the magnetic

field in the regime,  $Co = 1.6-2.4$  whereas close to the transition from anti-solar to solar rotation profiles, at  $Co = 2.6-2.8$  even systems with anti-solar rotation profiles produce clear cycles in their axisymmetric fields. This seems to be quite a robust finding, as this behavior persists even when the efficiency of convection is varied. Cyclic magnetic activity has been seen on stars that are postulated to have anti-solar differential rotation profiles (Weber et al. 2005; Kővári et al. 2007; Harutyunyan et al. 2016), which, according to our results, would be possible in a narrow region near the break-point from anti-solar/axisymmetric to solar/nonaxisymmetric behavior.

In the rapid rotation regime, both dominantly axisymmetric and nonaxisymmetric solutions produce oscillatory behavior of very different nature, which, however, occurs over similar time scales and produces similar magnitudes of variations, at least in terms of variations in the surface magnetic field strength. In the axisymmetric case, the oscillations relate to the latitudinal dynamo wave and are accompanied by a polarity change. In the majority of the nonaxisymmetric cases, the oscillations relate to the changing activity levels of active longitudes on different hemispheres with no associated polarity change. In one low-resolution case that produces only a very weak dynamo, we found a solution which also shows flip-flop type polarity reversals, but this particular parameter regime needs to be studied with high-resolution runs. The drift period of the active longitude system in the orbital frame of reference identified in almost every simulation seem to be de-coupled from the magnetic activity cycle, but together with the variations in the active longitude strengths can be thought to give rise to an azimuthal dynamo wave. Also observationally the occurrence of cycles is not related to the axisymmetry of the stellar magnetic fields. Activity cycles are observed on slow and fast rotating stars alike, regardless if they have active longitudes or not (Lehtinen et al. 2016).

Our results confirm the findings of Featherstone & Hindman (2016a) that the scale at which the power spectrum of the velocity field peaks shifts to higher values of  $\ell$  with increasing rotation speed, indicating the presence of smaller convective cells at rapid rotation. Our results have also demonstrated that sufficiently high numerical resolution is important for allowing the  $m = 1$  nonaxisymmetric structure to develop. The wedge assumption in the azimuthal direction was not found to be a good one for rapidly rotating stars, as it firstly suppresses the non-axisymmetric modes that emerge rather close to the solar rotation rate. Secondly, oscillatory solutions have previously not been found in wedges with anti-solar rotation profiles, while in this study such solutions could be found in the runs with full azimuthal extents. The magnetic structures appearing preferentially at high-latitude regions with more rapid rotation also put the latitudinal wedge assumption into a question. A better modelling strategy for the future are full spherical grids where the parameters are chosen so that the models are equally supercritical in terms of the Rayleigh number.

*Acknowledgements.* MV acknowledges postgraduate fellowship from the SOLSTAR Max Planck Research Group and having been enrolled in the International Max Planck Research School for Solar System Science at the University of Göttingen (IMPRS) framework. The simulations were performed using the supercomputers hosted by CSC – IT Center for Science Ltd. in Espoo, Finland, who are administered by the Finnish Ministry of Education. Special Grand Challenge allocation DYNAMO13 is acknowledged. J.W. acknowledges funding by the Max-Planck/Princeton Center for Plasma Physics and from the People Programme (Marie Curie Actions) of the European Union's Seventh Framework Programme (FP7/2007-2013) under REA grant agreement No. 623609. Financial support from the Academy of Finland grant No. 272157 to the ReSoLVE Centre of Excellence (JW,MJK,PJK), Finnish Cultural Foundation grant No. 00170789 (NO), as well as the NSF Astronomy and Astrophysics

Grants Program (grant 1615100), and the Research Council of Norway under the FRINATEK grant 231444 are acknowledged (AB).

## References

- Augustson, K., Brun, A. S., Miesch, M., & Toomre, J. 2015, *ApJ*, 809, 149
- Baliunas, S. L., Donahue, R. A., Soon, W. H., et al. 1995, *ApJ*, 438, 269
- Beaudoin, P., Simard, C., Cossette, J.-F., & Charbonneau, P. 2016, *ApJ*, 826, 138
- Berdyugina, S. V., Pelt, J., & Tuominen, I. 2002, *A&A*, 394, 505
- Berdyugina, S. V. & Tuominen, I. 1998, *A&A*, 336, L25
- Brandenburg, A. 2007, in *IAU Symp.*, Vol. 239, *IAU Symp.*, ed. F. Kupka, I. Roxburgh, & K. L. Chan, 457–466
- Brandenburg, A., Mathur, S., & Metcalfe, T. S. 2017, *ApJ*, 845, 79
- Brandenburg, A., Saar, S. H., & Turpin, C. R. 1998, *ApJ*, 498, L51
- Brown, B. P., Browning, M. K., Brun, A. S., Miesch, M. S., & Toomre, J. 2008, *ApJ*, 689, 1354
- Brown, B. P., Browning, M. K., Brun, A. S., Miesch, M. S., & Toomre, J. 2010, *ApJ*, 711, 424
- Busse, F. H. 1970, *ApJ*, 159, 629
- Busse, F. H. 2007, *Sol. Phys.*, 245, 27
- Chandrasekhar, S. 1961, *Hydrodynamic and hydromagnetic stability*
- Chen, C. 1988, *Signal Processing Handbook*, Electrical and Computer Engineering (Taylor & Francis)
- Cole, E., Brandenburg, A., Käpylä, P. J., & Käpylä, M. J. 2016, *A&A*, 593, A134
- Cole, E., Käpylä, P. J., Mantere, M. J., & Brandenburg, A. 2014, *ApJL*, 780, L22
- Distefano, E., Lanzafame, A. C., Lanza, A. F., Messina, S., & Spada, F. 2017, *A&A*, 606, A58
- Donati, J.-F. & Landstreet, J. D. 2009, *ARA&A*, 47, 333
- Fan, Y. & Fang, F. 2014, *ApJ*, 789, 35
- Featherstone, N. A. & Hindman, B. W. 2016a, *ApJ*, 830, L15
- Featherstone, N. A. & Hindman, B. W. 2016b, *ApJ*, 818, 32
- Gastine, T., Duarte, L., & Wicht, J. 2012, *A&A*, 546, A19
- Gastine, T., Yadav, R. K., Morin, J., Reiners, A., & Wicht, J. 2014, *MNRAS*, 438, L76
- Ghizaru, M., Charbonneau, P., & Smolarkiewicz, P. K. 2010, *ApJ*, 715, L133
- Gizon, L., Duvall, T. L., & Schou, J. 2003, *Nature*, 421, 43
- Green, C. A. & Kosovichev, A. G. 2006, *ApJ*, 641, L77
- Hackman, T., Lehtinen, J., Rosén, L., Kochukhov, O., & Käpylä, M. J. 2016, *A&A*, 587, A28
- Hackman, T., Pelt, J., Mantere, M. J., et al. 2013, *A&A*, 553, A40
- Hanasoge, S. M., Duvall, T. L., & Sreenivasan, K. R. 2012, *Proc. Natl. Acad. Sci.*, 109, 11928
- Harutyunyan, G., Strassmeier, K. G., Künstler, A., Carroll, T. A., & Weber, M. 2016, *A&A*, 592, A117
- Hotta, H., Rempel, M., & Yokoyama, T. 2014, *ApJ*, 786, 24
- Hotta, H., Rempel, M., & Yokoyama, T. 2016, *Science*, 351, 1427
- Ishihara, N. & Kida, S. 2000, *Journal of the Physical Society of Japan*, 69, 1582
- Järvinen, S. P., Korhonen, H., Berdyugina, S. V., et al. 2008, *A&A*, 488, 1047
- Jetsu, L. 1996, *A&A*, 314, 153
- Jetsu, L., Pelt, J., & Tuominen, I. 1993, *A&A*, 278, 449
- Käpylä, M. J., Käpylä, P. J., Olsper, N., et al. 2016, *A&A*, 589, A56
- Käpylä, P. J., Käpylä, M. J., & Brandenburg, A. 2014, *A&A*, 570, A43
- Käpylä, P. J., Käpylä, M. J., Olsper, N., Warnecke, J., & Brandenburg, A. 2017, *A&A*, 599, A5
- Käpylä, P. J., Mantere, M. J., & Brandenburg, A. 2011, *Astron. Nachr.*, 332, 883
- Käpylä, P. J., Mantere, M. J., & Brandenburg, A. 2012, *ApJ*, 755, L22
- Käpylä, P. J., Mantere, M. J., Cole, E., Warnecke, J., & Brandenburg, A. 2013, *ApJ*, 778, 41
- Karak, B. B., Käpylä, P. J., Käpylä, M. J., et al. 2015, *A&A*, 576, A26
- Kővári, Z., Bartus, J., Strassmeier, K. G., et al. 2007, *A&A*, 474, 165
- Kitchatinov, L. L. & Rüdiger, G. 1999, *A&A*, 344, 911
- Kochukhov, O., Mantere, M. J., Hackman, T., & Ilyin, I. 2013, *A&A*, 550, A84
- Krause, F. & Rädler, K.-H. 1980, *Mean-field Magnetohydrodynamics and Dynamo Theory* (Oxford: Pergamon Press)
- Lehtinen, J., Jetsu, L., Hackman, T., Kajatkari, P., & Henry, G. W. 2016, *A&A*, 588, A38
- Lindborg, M., Mantere, M. J., Olsper, N., et al. 2013, *A&A*, 559, A97
- Moss, D., Barker, D. M., Brandenburg, A., & Tuominen, I. 1995, *A&A*, 294, 155
- Moss, D. & Brandenburg, A. 1995, *Geophys. Astrophys. Fluid Dyn.*, 80, 229
- Nelson, N. J., Brown, B. P., Brun, A. S., Miesch, M. S., & Toomre, J. 2013, *ApJ*, 762, 73
- Oláh, K., Kővári, Z., Petrovay, K., et al. 2016, *A&A*, 590, A133
- Oláh, K., Kolláth, Z., Granzer, T., et al. 2009, *A&A*, 501, 703
- Olsper, N., Käpylä, M. J., Pelt, J., et al. 2015, *A&A*, 577, A120
- Ossendrijver, M. 2003, *A&A Rev.*, 11, 287
- Parker, E. N. 1955, *ApJ*, 121, 491
- Pelt, J., Brooke, J. M., Korpi, M. J., & Tuominen, I. 2006, *A&A*, 460, 875
- Pulkkinen, P. & Tuominen, I. 1998, *A&A*, 332, 748
- Rädler, K.-H., Wiedemann, E., Brandenburg, A., Meinel, R., & Tuominen, I. 1990, *A&A*, 239, 413
- Reinhold, T., Cameron, R. H., & Gizon, L. 2017, *A&A*, 603, A52
- Reinhold, T. & Gizon, L. 2015, *A&A*, 583, A65
- Reinhold, T., Reiners, A., & Basri, G. 2013, *A&A*, 560, A4
- Roettenbacher, R. M., Monnier, J. D., Korhonen, H., et al. 2016, *Nature*, 533, 217
- Rosén, L., Kochukhov, O., Hackman, T., & Lehtinen, J. 2016, *A&A*, 593, A35
- Rüdiger, G. 1978, *Astron. Nachr.*, 299, 217
- Saar, S. H. & Brandenburg, A. 1999, *ApJ*, 524, 295
- Schrinner, M., Petitdemange, L., & Dormy, E. 2012, *ApJ*, 752, 121
- See, V., Jardine, M., Vidotto, A. A., et al. 2016, *MNRAS*, 462, 4442
- Stassun, K. G., Hebb, L., Covey, K., et al. 2011, in *Astronomical Society of the Pacific Conference Series*, Vol. 448, 16th Cambridge Workshop on Cool Stars, Stellar Systems, and the Sun, ed. C. Johns-Krull, M. K. Browning, & A. A. West, 505
- Strugarek, A., Beaudoin, P., Charbonneau, P., Brun, A. S., & do Nascimento, J.-D. 2017, *Science*, 357, 185
- Warnecke, J., Käpylä, P. J., Käpylä, M. J., & Brandenburg, A. 2014, *ApJ*, 796, L12
- Warnecke, J., Käpylä, P. J., Käpylä, M. J., & Brandenburg, A. 2016, *A&A*, 596, A115
- Warnecke, J., Rheinhardt, M., Käpylä, P. J., Käpylä, M. J., & Brandenburg, A. 2017, *A&A*, submitted, arXiv:1601.03730
- Weber, M., Strassmeier, K. G., & Washuettl, A. 2005, *Astron. Nachr.*, 326, 287
- Yadav, R. K., Gastine, T., Christensen, U. R., & Reiners, A. 2015, *A&A*, 573, A68